PHYSICAL REVIEW D **88,** 044055 (2013)

De Sitter universe from causal dynamical triangulations without preferred foliation

S. Jordan* and R. Loll†

Radboud University Nijmegen, Institute for Mathematics, Astrophysics and Particle Physics, Heyendaalseweg 135, NL-6525 AJ Nijmegen, Netherlands

(Received 27 July 2013; published 30 August 2013)

We present a detailed analysis of a recently introduced version of causal dynamical triangulations that does not rely on a distinguished time slicing. Focusing on the case of $2 + 1$ spacetime dimensions, we analyze its geometric and causal properties, present details of the numerical setup, and explain how to extract "volume profiles." Extensive Monte Carlo measurements of the system show the emergence of a de Sitter universe on large scales from the underlying quantum ensemble, similar to what was observed previously in standard causal dynamical triangulation quantum gravity. This provides evidence that the distinguished time slicing of the latter is not an essential part of its kinematical setup.

DOI: 10.1103/PhysRevD.88.044055 PACS numbers: 04.60.Gw, 04.60.Nc

I. INTRODUCTION

First attempts in the 1990s to define quantum gravity nonperturbatively with the help of dynamical triangulations (DTs) were based on an intrinsically Euclidean path integral, whose configuration space consists of four-dimensional, curved Riemannian spaces. DT works with a regularized version of this space in terms of triangulations, piecewise flat spaces of positive definite metric signature. Its elementary building block is a four-simplex, a generalization to four dimensions of a triangle (two-simplex) and a tetrahedron (three-simplex). An individual building block is a piece of flat four-dimensional Euclidean space and therefore does not carry any curvature. However, numerical investigations of the nonperturbative dynamics of DT quantum gravity found that it has neither a large-scale limit compatible with general relativity [1–3] nor a second-order phase transition allowing for a continuum limit in the sense of lattice quantum field theory [4,5]. Despite the negative nature of this result, the fact that the model contains criteria which could be used for its falsification should be appreciated. For many other candidate theories of quantum gravity, this is not obviously the case.

Causal dynamical triangulations (CDT) were introduced in Ref. [6] in an attempt to overcome these problems. The key new idea of CDT is to incorporate aspects of the *causal structure* of classical general relativity at a more fundamental level into the nonperturbative gravitational path integral.[1] The elementary building blocks of CDT quantum gravity are flat four-simplices of *Lorentzian* signature, that is, pieces of Minkowski space. The carrier space of the corresponding path integral consists of piecewise flat simplicial manifolds assembled from these building blocks. In addition, each path integral history has a distinguished discrete foliation and an associated notion of (discrete) proper time, which ensures the presence of a well-defined causal structure globally (see Refs. [7,8] for details on motivation, construction, and results in CDT). Numerical simulations in $3 + 1$ dimensions have shown that these modifications lead to a completely different quantum dynamics, compared to the earlier Euclidean DT model: CDT quantum gravity in $3 + 1$ dimensions contains a phase whose nonperturbative ground state of geometry is extended, macroscopically four-dimensional, and on large scales can be matched to a de Sitter universe [9,10]. Moreover, the theory has recently been shown to possess a second-order phase transition, which according to standard arguments is a prerequisite for the existence of a continuum limit [11].

The causal structure of CDT is realized by putting together its simplicial building blocks such that each CDT configuration has a product structure, not just at the level of topology—usually chosen as $[0, 1] \times {}^{(3)}\Sigma$, for fixed three-topology ${}^{(3)}\Sigma$—but *as triangulations*. A $(3 + 1)$-dimensional CDT geometry consists of a sequence of slabs or layers, each of thickness 1, which may be thought of as a single unit of proper time. The orientation of the light cones of all four-simplices in a given slab is consistent with this notion of time. In this way the causal structure becomes linked to a preferred discrete foliation of spacetime.

To understand better how the preferred time foliation on the one hand and the causal structure on the other contribute to the evidence of a good classical limit—the key distinguishing feature of CDT quantum gravity—it would be highly desirable to disentangle these two elements of "background structure." We recently proposed a modification of standard CDT which does exactly that [12]. The main idea, applicable in any spacetime dimension d, is to enlarge the set of d-simplices by new types of simplicial building blocks, also pieces of d-dimensional Minkowski space, but with different link-type assignments and therefore a different orientation of the light cone relative to the boundaries of the simplex. Including the new building blocks is in general not compatible with the preferred foliation of CDT. Nevertheless, with a suitable choice of

*s.jordan@science.ru.nl
†r.loll@science.ru.nl

[1]By contrast, Euclidean gravity does not distinguish between space and time and therefore has no causal structure and no notion of causality.

 © 2013 American Physical Society

gluing rules one, can still obtain Lorentzian simplicial manifolds with a well-defined causal structure, at least locally. In this way the issue of causality becomes dissociated from the notion of a preferred foliation. The interesting question is then whether the quantum-gravitational model using "nonfoliated CDT" can reproduce the results of the standard formulation, especially those concerning the large-scale properties of quantum spacetime. The main conclusion of the present paper, previously announced in Ref. [12], is that it *can*, at least in spacetime dimension $2 + 1$. At least in higher dimensions, this result appears to weaken the potential link of CDT quantum gravity with Hořava—Lifshitz gravity [13,14], where the presence of a preferred foliation is a key ingredient.[2]

To summarize, our intention is to get rid of the *distinguished* foliation (and associated discrete time label t) of CDT, whose leaves for integer t coincide with simplicial spatial hypermanifolds consisting entirely of *spacelike* subsimplices of codimension 1. This does not mean that the nonfoliated CDT configurations cannot in principle be foliated with respect to some continuous notion of time but only that there is in general no canonical way of doing this in terms of a distinguished substructure of the triangulated spacetimes.

Of course, having *a* notion of time at the level of the regularized geometries is important. In the standard formulation of CDT, we get a notion of (discrete proper) time t for free, simply by counting consecutive "slabs," as described earlier. The presence of this time label allows us to define a transfer matrix and an associated propagator with the correct behavior under composition (whose continuum limit in dimension $1 + 1$ can be computed analytically [6]) and prove a version of reflection positivity [16]. Yet another advantage of having an explicit time variable is that we can construct observables like the volume profile, which measures the distribution of spatial volume as a function of time. The analysis of these volume profiles in $3 + 1$ dimensions has been crucial in relating the large-scale behavior of CDT to a de Sitter cosmology in the continuum [10,17].[3]

By contrast, in the enlarged CDT setup we will be considering, typical triangulations will be more complicated, in the sense that the purely spatial subsimplices of codimension 1 will no longer align themselves into a neat sequence of simplicial *hypermanifolds* but instead will form branching structures, as will be explained in more detail below. This also implies that we no longer have a distinguished time variable at our disposal. Nevertheless, as we shall demonstrate for the nontrivial case of $2 + 1$ dimensions, it is possible to construct a meaningful time variable, whose restriction to standard, nonbranching CDT configurations agrees with the usual proper time label t. This will enable us to extract volume profiles from the numerical simulations and compare their dynamics with that of the standard formulation.

There is a number of good reasons for beginning our investigation in $2 + 1$ dimensions, as we are doing in the present work. In standard CDT, the large-scale properties of the quantum universe generated by the nonperturbative quantum dynamics are qualitatively very similar to those in $3 + 1$ dimensions and are well described by a (three-dimensional) Euclidean de Sitter universe [18,19]. Furthermore, as we will describe in Sec. VI, the nonfoliated CDT model requires new Monte Carlo moves, which are significantly more difficult to implement than the generalized Pachner moves used in standard CDT. Writing the simulation software for the new model becomes a very challenging task already in $2 + 1$ dimensions. At the same time, the increased complexity of the simulation software leads to longer simulation times. It is not even clear currently whether analogous simulations in $3 + 1$ dimensions could be performed with acceptable running times using contemporary simulation hardware.

Before embarking on our exploration of the dynamics of nonfoliated CDT, let us comment briefly on prior work, which considered explicitly a possible relaxation of CDT's strict time slicing.[4] A soft way of relaxing the foliation in $1 + 1$ dimensions was studied in Ref. [21], where under certain conditions the timelike links were allowed to have varying length. In this approach the foliation is still present, since the connectivity of the underlying triangulation is unchanged, but the individual leaves of the foliation are not placed at equidistant intervals. The authors argued that this should not affect the continuum limit of the model. A similar idea in $2 + 1$ dimensions was considered in Ref. [22], where it was also suggested to add new elementary building blocks to CDT, which extend over two slabs of the foliation instead of one. This study did not include details of how the path integral of the corresponding generalization of CDT quantum gravity should be formulated or simulated.

The remainder of this article is structured as follows. We begin with a brief review of causal dynamical triangulations in Sec. II. In Sec. III we discuss aspects of CDT without preferred foliation in $1 + 1$ dimensions, to illustrate the basic geometric idea behind the enlarged model. Section IV contains a detailed study of the kinematical

[2]This differs from $1 + 1$ dimensions, where CDT is a quantum-mechanical system of a single length variable and has been shown to coincide with projectable Hořava–Lifshitz gravity [15].

[3]One does not know *a priori* whether t or any other time label of the regularized model will assume a distinguished physical role in the continuum theory; this can only be determined by studying suitable continuum *observables*, like the volume profiles.

[4]In CDT in $1 + 1$ dimensions, one can rederive the exact continuum propagator without invoking an explicit proper-time slicing (see, for example, Ref. [20]). It is unclear how to generalize such a construction to higher dimensions.

aspects of nonfoliated CDT in 2 + 1 dimensions. Section V deals with actions and the Wick rotation, and Sec. VI summarizes the new numerical setup. This includes an overview of the Monte Carlo moves in 2 + 1 dimensions, a prescription for how a notion of time can be defined on the quantum ensemble and how the corresponding volume profiles can be extracted. In Sec. VII we explore the phase diagram of the model numerically. In Sec. VIII we study distributions of tetrahedra as a function of the coupling constants, which allows us to understand how foliated (in the sense of regular CDT) typical configurations are. The results of our analysis of the volume profiles and their matching to a de Sitter universe are presented in Sec. IX and our conclusions in Sec. X. Further details on the numerical implementation as well as a documentation of the relevant software can be found in Ref. [23].

II. REVIEW OF CAUSAL DYNAMICAL TRIANGULATIONS

To set the stage for our subsequent generalization, we recall in the following some elements of causal dynamical triangulations, mainly based on the original literature on CDT in 1 + 1 [6], 2 + 1 [18], and 3 + 1 dimensions [9,10]. For more extensive reviews and lecture notes on CDT, we refer the interested reader to Refs. [7,8,24].

The central object of interest in the CDT approach to quantum gravity is the gravitational path integral, which in the continuum can be written formally as

$$Z(G,\Lambda) = \int_{\text{geometries }[g]} \mathcal{D}[g] \exp\left(iS_{\text{EH}}[g]\right), \qquad (1)$$

where $S_{\text{EH}}[g]$ is the Einstein–Hilbert action, written as a functional of the metric g, $\mathcal{D}[g]$ is a measure on the space of geometries (the space of equivalence classes $[g]$ of metrics under the action of the diffeomorphism group), G is Newton's constant, and Λ is the cosmological constant. To define the path integral properly, it needs to be regularized, which in CDT is done by performing the "sum over histories" (1) over a set of piecewise flat, simplicial Lorentzian geometries—in other words, triangulations—effectively discretizing the curvature degrees of freedom of spacetime. The way in which triangulations encode curvature is illustrated best in two dimensions. In the Euclidean plane, consider a flat disk consisting of six equilateral triangles which share a central vertex, and remove one of the triangles (Fig. 1, left). By identifying the opposite sides of the gap thus created, the piecewise flat disk acquires nontrivial (positive Gaussian) curvature, whose magnitude is equal to the deficit angle $\pi/3$ at the vertex (Fig. 1, right). This also coincides with the rotation angle undergone by a two-dimensional vector parallel transported around the vertex and is therefore an *intrinsic* property of the two-dimensional disk. The principle of encoding curvature through deficit angles (located at subsimplices of dimension $d-2$ in a d-dimensional triangulation) works in any dimension and for any metric signature.

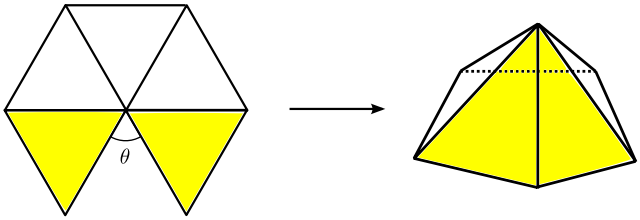

FIG. 1 (color online). A disk in the flat Euclidean plane is triangulated in terms of six equilateral triangles, one of which is subsequently removed (left). Regluing the remaining triangles, one obtains a disk with positive curvature, characterized by a deficit angle $\theta = \pi/3$ and independent of the embedding space (right).

Let us review the difference between the (Euclidean) DT and the (Lorentzian) CDT path integral, again for simplicity in dimension two. Recall that the geometric properties of a flat triangle (or, in higher dimensions, a flat simplex) are completely determined by the lengths of its edges,[5] including the *signature* of the flat metric in the building block's interior. In the Euclidean DT approach in two dimensions, one works with a single type of building block, an equilateral triangle of Euclidean signature, all of whose edges have some fixed spacelike length, the same length for all triangles in the triangulation. As we have seen above, the number of such triangles around each interior vertex of the triangulation characterizes the local curvature at that vertex. In this way the formal integral over curved geometries in the continuum path integral (1) is turned into a sum over triangulations, typically subject to some manifold conditions, which ensure that the triangulation looks like a two-dimensional space everywhere.

By contrast, the flat triangles used in CDT quantum gravity have Lorentzian signature, something that cannot be achieved for equilateral triangles. The standard choice of an elementary CDT building block in 1 + 1 dimensions is one whose base has squared length $\ell_s^2 > 0$ (and therefore is spacelike) and whose remaining two edges both have squared length $\ell_t^2 < 0$ (and therefore are timelike). From the point of view of triangulating Lorentzian spacetimes, one could in principle have chosen ℓ_t^2 to be space- or lightlike, but then CDT's prescription of a Wick rotation—to be described below—would no longer be applicable.

Figure 2 illustrates the fundamental building blocks of two-dimensional DT (left) and CDT (right) and how they are put together to obtain piecewise flat manifolds of Euclidean and Lorentzian signature. The two-dimensional graphs correctly represent the neighborhood relations of adjacent triangles, but not the actual length assignments, since it is impossible to flatten out a curved surface and preserve the edge lengths at the same time. Note that in

[5]To treat space-, time-, and lightlike edges on the same footing, it is convenient to work with the *squared* edge lengths.

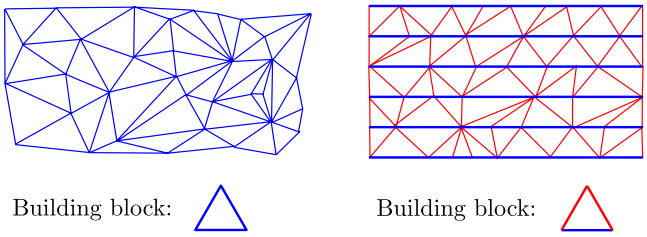

FIG. 2 (color online). Two-dimensional triangulations: from Euclidean DT, consisting of equilateral triangles with Euclidean signature (left), and from Lorentzian CDT, constructed from Minkowskian triangles with one spacelike and two timelike links (right). In both cases, curvature is present at all interior vertices whose coordination number (number of triangles meeting at the vertex) is not six. Timelike links are shown in red and spacelike ones in blue.

the Lorentzian case, the spacelike edges form a sequence of one-dimensional simplicial submanifolds, which can be interpreted as hypermanifolds of constant time $t = 0, 1, 2, \ldots$, endowing each triangulation with a distinguished notion of (proper) time. This time can be extended continuously to the interior of all triangles [25].

The ensemble of spacetimes forming the carrier space of the CDT path integral are all triangulations which consist of a fixed number t_{tot} of triangulated strips $\Delta t = 1$, where each strip is an arbitrary sequence of up and down triangles between times t and $t + 1$. The topology of space (usually chosen to be S^1) is not allowed to change in time; that is, branchings into multiple S^1 universes are forbidden. It was shown in Ref. [26] that the global foliation of a $1 + 1$-dimensional CDT spacetime into such strips can be understood as consequence of a *local* regularity condition, namely, that precisely two spacelike edges be incident on any vertex. Note that these geometries are causally well behaved and obey a piecewise linear analogue of global hyperbolicity.

As already described in the introduction, the idea of creating individual path integral configurations with a well-behaved causal structure by imposing a preferred foliation on the underlying simplicial manifold is also realized in CDT in higher dimensions. Figure 3 shows part of a $2 + 1$-dimensional CDT spacetime. Each leaf at integer t of

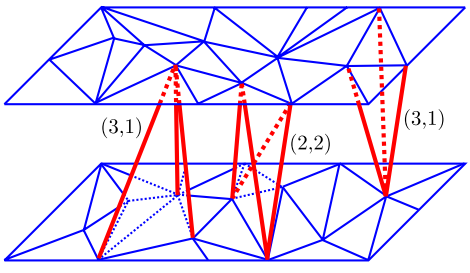

FIG. 3 (color online). Two adjacent spatial slices in a piece of foliated CDT triangulation in $2 + 1$ dimensions. Tetrahedra of both types are shown.

the foliation forms a two-dimensional triangulation of the same fixed topology ${}^{(2)}\Sigma$ and consists of equilateral spacelike triangles with link length ℓ_s. Adjacent triangulated spatial hypermanifolds are connected using Lorentzian tetrahedra to form a $2 + 1$-dimensional simplicial manifold with spacetime topology $[0, 1] \times {}^{(2)}\Sigma$, which again is a sequence of t_{tot} triangulated slabs $\Delta t = 1$. Each such geometry comes with a time label t, which can be defined continuously throughout the triangulation, and for integer values coincides with the discrete labeling of the simplicial leaves just described [25]. For reasons of simplicity, in the simulations time is often compactified. The topology then becomes $S^1 \times {}^{(2)}\Sigma$.

The fundamental building blocks of three-dimensional CDT quantum gravity are flat Minkowskian tetrahedra, whose geometric properties are determined by their edge lengths. As in $1 + 1$ dimensions, one considers two different link lengths, one spacelike with squared length ℓ_s^2 and one timelike with $\ell_t^2 = -\alpha \ell_s^2$. Without loss of generality, we have introduced here a positive constant α, which quantifies the relative magnitude of space- and timelike edge lengths and in what follows will be referred to as the *asymmetry parameter*.

CDT path integral configurations are assembled from two different tetrahedron types, which can be distinguished by their orientation with respect to the preferred foliation. As can be seen from Fig. 3, spacelike edges of a tetrahedron are always contained in a spatial submanifold of integer t, whereas timelike edges always connect different spatial slices. The (3, 1)-tetrahedron has three spacelike links forming a spacelike triangle, while the (2, 2)-tetrahedron contains only two spacelike links. The notation (i, j) indicates that i vertices of the tetrahedron are located on one spatial slice and the remaining j vertices on an adjacent one.

The kinematical setup of CDT quantum gravity in $3 + 1$ dimensions can be defined in a similar way. The leaves of the preferred foliation are three-dimensional Euclidean triangulations of fixed topology, and neighboring slices are connected using Minkowskian four-simplices. Path integral configurations are simplicial manifolds assembled from two types of these building blocks, denoted by (4, 1) and (3, 2), depending on how their vertices are distributed among adjacent spatial slices. By labeling the foliation with increasing integers, we again get a time variable for free, with every vertex being assigned a definite discrete time label.

Another ingredient that needs to be specified to make the model complete is an implementation on piecewise flat geometries of the Einstein–Hilbert action in the path integral (1), which in CDT quantum gravity is done following Regge's prescription [27]. One should point out that models of the type we are studying tend to be very robust with respect to changes in the precise form of the action (which obviously is subject to discretization ambiguities)

and of the configuration space, in the sense that a wide range of different regularizations and kinematical ingredients will lead to the same continuum physics, if the latter can be defined meaningfully. An exception to this is of course the imposition of causality constraints, which distinguishes CDT from DT quantum gravity and leads in all dimensions studied so far to genuinely different continuum results. In two dimensions, this can be demonstrated exactly, for example, by comparing specific observables and critical exponents, since the CDT model can be solved analytically [6]. In higher dimensions, information about the behavior of observables comes primarily from numerical simulations; three-dimensional CDT quantum gravity has only been solved partially and for restricted classes of triangulations [28], while in four dimensions analytical methods are mostly unavailable, and one must resort to Monte Carlo simulations to extract physical results.

In order to analyze the dynamics of CDT quantum gravity using such simulations, a Wick rotation must be performed to convert the complex path integral amplitudes to real Boltzmann weights. This can be achieved by performing an analytic continuation of the asymmetry parameter by rotating it in the lower half of the complex plane such that α is mapped to $-\alpha$ [16]. As a consequence, the gravitational path integral becomes a statistical partition function of the form

$$Z = \sum_{T\in\mathcal{C}} \frac{1}{C(T)} \exp\left(-S^{\mathrm{eucl}}_{\mathrm{Regge}}(T)\right), \tag{2}$$

where $\mathcal{C}$ is the space of all causal, Lorentzian triangulations T, $S^{\mathrm{eucl}}_{\mathrm{Regge}}$ the Euclideanized Regge action, and $1/C(T)$ the discrete analog of the path integral measure, with $C(T)$ denoting the order of the automorphism group of T. In Sec. V below, we will derive and discuss the explicit functional form of the Regge implementation of the three-dimensional Einstein–Hilbert action in terms of the triangulation data and the coupling constants of the nonfoliated CDT model.

III. RELAXING THE FOLIATION: 1 + 1 DIMENSIONS

As a warm-up for the three-dimensional case, we will in this section illustrate our general strategy for relaxing the distinguished foliation by discussing the situation in 1 + 1 dimensions. The key idea is to add new elementary Minkowskian building blocks, while sticking to two types of links, one spacelike and one timelike, where we will continue to use the notation ℓ_s^2 and $\ell_t^2 = -\alpha\ell_s^2$ for their squared lengths. Figure 4 shows the four types of triangles which can be built from these two link types. By calculating the metric inside the triangles, one finds that there are exactly two which have Lorentzian signature $(-+)$, the two at the center of the figure. We will call them the *sst*- and the *tts*-triangle, respectively, in reference to the spacelike (s) and timelike (t) edges they contain. Note that in standard CDT in two dimensions, only the *tts* triangle is used.

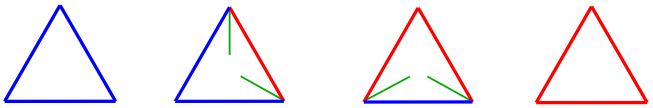

FIG. 4 (color online). The four triangle types which can be constructed from using just two link lengths, spacelike (blue) and timelike (red). Only the two Minkowskian triangles (of types *sst* and *tts*) at the center have the correct signature for triangulating two-dimensional Lorentzian spacetimes. The green lines inside the Lorentzian triangles indicate light rays through the corner vertices.

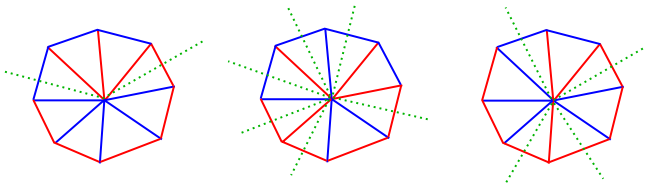

FIG. 5 (color online). Three examples of vertex neighborhoods in 1 + 1 dimensions. Causality is violated at the central vertex whenever the number of light cones is not two (left and center). At a causally well-behaved vertex, one crosses exactly two light cones (equivalently, four lightlike directions) when going around the vertex (right).

The use of Lorentzian building blocks is not a sufficient condition for the triangulation to have a well-defined causal structure locally; we also need to check that we obtain well-defined light cones in points where triangles are glued together. If the gluing happens according to the standard rule of only identifying links of the same type (spacelike with spacelike, timelike with timelike), the only local causality violations[6] can occur at the vertices of the triangulation. Counting past and future light cones separately, the point is that one may obtain more or fewer than the required two light cones at a vertex, as illustrated by the local neighborhoods depicted in Fig. 5. Local causality implies crossing exactly two light cones when going around a vertex or, equivalently, crossing exactly four lightlike lines emanating radially from the vertex.

As a next step, we will consider the global causal structure of individual triangulated manifolds satisfying the local vertex causality condition everywhere. This global structure will in general depend on the chosen topology. For simplicity, we will restrict ourselves to the cases $[0,1]\times S^1$ (space is a compact circle) and $[0,1]\times[0,1]$

[6]Whenever we talk about geometries being *causal*, what we have in mind is that they possess a well-behaved causal structure. This should not be confused with the notion of causality in standard (quantum) field theory, which refers to the behavior of matter fields on a given background that typically already comes with a fixed causal structure.

(space is a closed interval), where the initial and final boundary are assumed to be spacelike and any other boundaries (in the second case) timelike. We will call such a spacetime globally causal if it does not contain any closed timelike curves. A "timelike curve" for our purposes will be a sequence of oriented, timelike links in a triangulation. Since the interior of every Minkowskian triangle has a well-defined light cone structure, a choice of orientation (i.e., a choice of which one is the past and which one the future light cone) induces an orientation on its timelike edges, which can be captured by drawing a future-pointing arrow onto the edge. Conversely, these arrow assignments fix the orientation of the triangle uniquely. To follow the "flow of time" in a triangulation, it is convenient to also associate a future-pointing arrow with each spacelike edge, which is drawn perpendicular to the edge; see Fig. 6.

Choosing a consistent orientation for all building blocks in standard CDT in this way is completely straightforward: each triangle sits in a strip between discrete times t and $t + 1$, which fixes its orientation uniquely. Independent of the spatial boundary conditions, there are no closed timelike curves (unless we impose periodic boundary conditions *in time*, which trivially makes any timelike curve closed, a situation we are not considering here).

By contrast, the situation in nonfoliated CDT is slightly more involved. Given a time-oriented triangle, the orientation of a neighboring triangle that shares an edge with the first one is uniquely determined by consistency. It is easy to see that when vertex causality is violated (like in the example of Fig. 5, left), inductively assigning orientations in this way will fail—i.e., lead to contradictions—even for a local vertex neighborhood. If vertex causality is satisfied, one can show that for noncompact spatial topology, there are no closed timelike curves [29]. For compact spatial slices, where the spacetime topology is that of a cylinder, one can construct explicit geometries which exhibit noncontractible, closed timelike curves. Of course, we do not know *a priori* whether the presence of closed timelike curves in individual path integral configurations has any influence on the continuum limit of the model and perhaps leads to undesirable continuum properties. It appears that in the context of our present investigation, this issue is largely circumvented. Although the causality conditions we impose are of a local nature, and may admit the presence of closed timelike curves, it turns out that the geometries dominating the sum over histories dynamically retain a weak degree of foliation (see Sec. VIII below), which suggests that such curves are certainly not abundant. We have not seen closed timelike curves in random samples but have not systematically tested for their presence either.

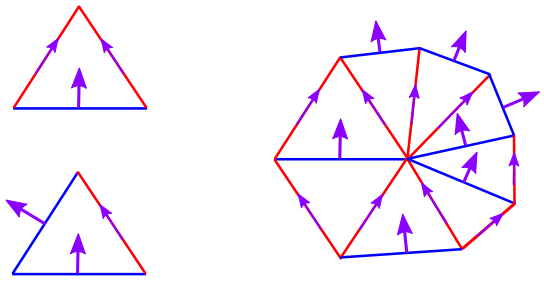

FIG. 6 (color online). Two Lorentzian triangles with consistent assignments of future-pointing arrows to its edges, as explained in the text (left). The time orientation of a given triangle determines the time orientation of its direct neighbors (right).

Anticipating the choice of boundary conditions we will make in $2 + 1$ dimensions, we may relax the local causality constraint slightly by allowing for the presence of an isolated "source" and "sink" of time. By this we mean a vertex where only timelike links meet, all of them either time oriented away from the vertex (source) or toward it (sink), as illustrated by Fig. 7. For compact spatial boundary conditions, choosing a source and a sink as initial and final (degenerate spatial) boundaries will convert the cylinder into a spherical S^2-spacetime topology. A similar choice of boundary conditions in $2 + 1$ dimensions will lead to a S^3-spacetime topology, with the source and sink forming the south and north pole of the sphere, as we will see later.

There is a particular substructure of the triangulations, called a *bubble* [29], which involves the newly added building blocks and is helpful in analyzing the geometry of nonfoliated CDT. In $1 + 1$ dimensions it is simply a pair of *sst* triangles with a chain of *tts* triangles in between. This is the general structure of a two-dimensional connected region bounded by a closed loop of spacelike links, and whose interior contains only timelike links, as shown in Fig. 8, left (we are assuming that vertex causality is satisfied everywhere). This should be contrasted with the structure of a strip, which likewise denotes a two-dimensional piece of triangulations bounded by spacelike links and without spacelike links in its interior but whose boundary is disconnected (Fig. 8, right). CDT quantum

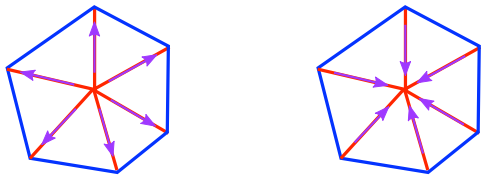

FIG. 7 (color online). A source and a sink of time in $1 + 1$ dimensions. In both cases, vertex causality is violated at the central vertex.

FIG. 8 (color online). A bubble (left) and a strip configuration (right) in $1 + 1$ dimensions.

gravity in 1 + 1 dimensions has only strips, whereas the version without distinguished foliation has both strips and bubbles. Analogous structures will play a role in our analysis in 2 + 1 dimensions, too, where also the interior structure of a bubble can become more complicated.

IV. RELAXING THE FOLIATION: KINEMATICS IN 2 + 1 DIMENSIONS

A. Local causality conditions

Following an analogous procedure in 2 + 1 dimensions to arrive at a model without distinguished simplicial hypermanifolds, we first must determine which flat tetrahedra—again only built from two types of edge lengths—give rise to Minkowskian building blocks of the correct Lorentzian signature $(-++)$. Figure 9 shows all types of tetrahedra which can be constructed using space- and timelike links with fixed squared lengths ℓ_s^2 and $\ell_t^2 = -\alpha\ell_s^2$, respectively. In the rest of this document, we will set $\ell_s = 1$. By calculating the metric in the interior of each tetrahedron type, one finds that only T_2, T_3, T_5, and T_9 have the required signature for all values $\alpha > 0$ of the asymmetry parameter and type T_7 only for $0 < \alpha < 1$. Note that standard CDT quantum gravity only uses the tetrahedra T_5 and T_9, in Sec. II referred to as (3,1)- and (2,2)-tetrahedra, respectively. In the present work, we will for reasons of simplicity investigate the version of the model where causal spacetimes are assembled from the tetrahedral types T_2, T_3, T_5, and T_9 (without T_7). As we will see, this already serves our purpose of breaking up the fixed foliated structure.

In 2 + 1 dimensions violations of local causality—which should therefore be forbidden by the gluing rules—can in principle occur at the links and the vertices of a triangulation. To check whether the light cone structure at a given link is well-behaved, it is sufficient to consider the geometry of a two-dimensional piecewise flat surface orthogonal to the link at its midpoint. This geometry is completely characterized by the set of tetrahedra sharing the link, the so-called star of the link (Fig. 10, center). Each tetrahedron in the star contributes a dihedral angle, defined by the intersection of the tetrahedron with the plane perpendicular to the link (Fig. 10, left). The plane segments spanned by all the dihedral angles associated to the given link form a new plane,[7] as shown in Fig. 10 (right).

We can distinguish between two cases. If the link at the center of the star is timelike, the metric of the plane has Euclidean signature, all dihedral angles are Euclidean, and there are no further causality conditions to be satisfied. If on the other hand the link is spacelike, the orthogonal plane is Lorentzian, and so are the dihedral angles. Like in the 1 + 1 dimensional case discussed in the previous section, we must then require that there is exactly one pair of light cones at the central vertex and that we encounter exactly four lightlike directions when circling around it. We say that the triangulation satisfies *link causality* if this condition is satisfied for every spacelike link.

Link causality guarantees that light cones everywhere in the triangulation are regular, except possibly at vertices. Intersecting the light cone(s) at a vertex V with the surface of a unit ball around V, we obtain two disconnected circles if and only if local causality holds at V; see Fig. 11 (left). In terms of the triangulated surface $\mathcal{S}$ of the unit neighborhood around V, vertex causality can be characterized as follows. Mark the end of a timelike link between V and $\mathcal{S}$ by a red dot and that of a spacelike one by a blue dot. In addition, whenever the light cone through V crosses a link on $\mathcal{S}$, mark the link with a green dot. Recalling the situation depicted in Fig. 4, it is clear that a green dot will always occur on a surface link which connects a red and a blue dot. If we cut all links that are marked with a green dot, the surface triangulation will break up into a number of connected components. If two of the components thus obtained contain red vertices and one component contains blue vertices, we say that *vertex causality* holds at V. If this is true for all vertices, we say that the triangulation satisfies vertex causality. We have not found any Monte Carlo moves which destroy vertex causality but maintain link causality. Also, we have not been able to explicitly construct a triangulation that satisfies link causality and violates vertex causality, but we do not currently have a proof that link causality implies vertex causality.

In order to compute the explicit action for the generalized CDT model of 2 + 1 dimensional quantum gravity, we will need the values of all dihedral angles. As usual, we will use Sorkin's complex angle prescription [30] for the latter, which conveniently keeps track of both Euclidean and Lorentzian angles. The analytic expressions for the cosines and sines of the dihedral angles are listed in Table I, from which the angles can be computed uniquely. Closer inspection of the geometry of the tetrahedra reveals that a dihedral angle contains a light cone crossing whenever the two triangles bounding the angle are a pair of a spacelike (Euclidean) and a Lorentzian triangle. Local link causality therefore implies that the triangle type changes exactly four times between spacelike and nonspacelike when we circle around a spacelike link once. The number of light cone crossings in the case of a Lorentzian angle is also contained in the table.

Just like in 1 + 1 dimensions, choosing a time orientation for a tetrahedron induces an orientation on its timelike links, as well as on the normal to any of its spacelike triangles. It is operationally convenient to keep track of these data in terms of future-oriented arrow assignments, as illustrated by Fig. 12. Again, the local causality conditions do not guarantee that the time orientation can be extended to the full triangulation. In addition to these conditions, we

[7]This is a slight misnomer; in general, this "plane" will not be flat because the vertex at the center will carry a nonvanishing deficit angle.

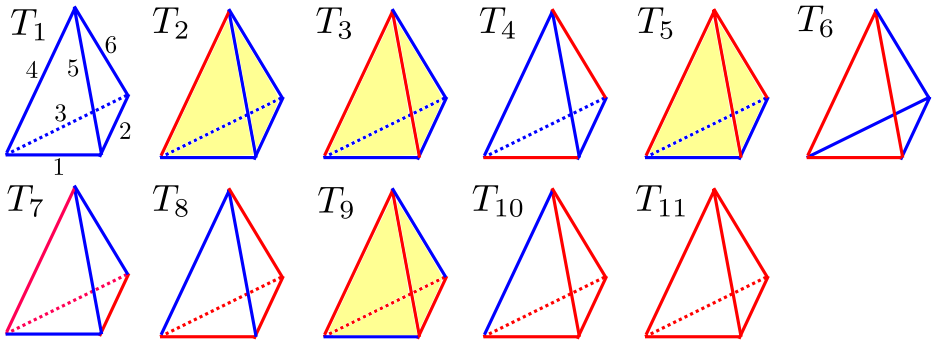

FIG. 9 (color online). All tetrahedra in $2+1$ dimensions that can be constructed from time- and spacelike links of fixed squared length, allowing for any signature. The tetrahedra highlighted in yellow have the correct Lorentzian signature; for the T_7 tetrahedron, this only holds for $\alpha < 1$. The link labeling shown for the first tetrahedron will be used for the other tetrahedra, too.

will therefore require (and enforce by way of our computer algorithm) that the complete triangulation can be time oriented consistently.

B. Simplicial substructures

In trying to understand the local geometry of nonfoliated CDT configurations and how it is affected by the Monte Carlo moves defined in Sec. VI below, it is useful to isolate specific local substructures built from the fundamental tetrahedra of Fig. 12. To start with, note that only tetrahedra of type T_2 and T_3 contain triangles with exactly two spacelike edges. Furthermore, both tetrahedra have exactly two such triangles. If we glue two of them together along such a triangle, the resulting simplicial complex again has two such triangles on its boundary. Iterating this gluing procedure, we end up with a chain of tetrahedra of type T_2 and T_3. We conclude that in a triangulation without boundary, the set of all tetrahedra of type T_2 and T_3 necessarily organizes itself into a collection of closed

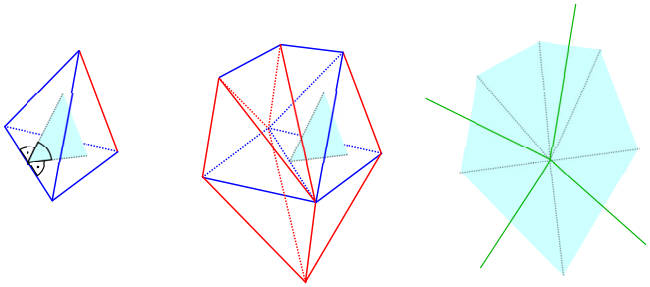

FIG. 10 (color online). Dihedral angle at the link with label "2" of a T_2 tetrahedron (left). Star of a link, all of whose tetrahedra contribute dihedral angles at the link (center). Two-dimensional cut perpendicular to the link. In the case depicted, the space is Lorentzian, with green lines representing light rays originating at the center (right).

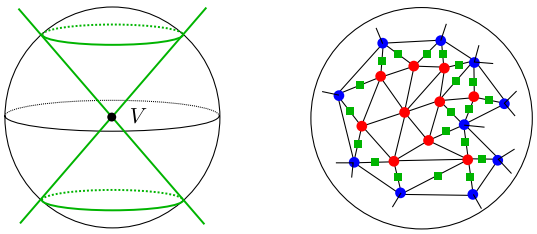

FIG. 11 (color online). In a triangulation obeying vertex causality, intersecting the boundary of a spherical vertex neighborhood with the light cones at the vertex V results in two disconnected circles (left). Part of the surface triangulation of a unit ball around V, showing timelike radial links as red, spacelike ones as blue, and light cone crossings as green dots (right).

TABLE I. Dihedral angles Θ for all tetrahedra types, given in terms of their trigonometric functions. The link numbers refer to the numbering given in Fig. 9. For Lorentzian angles, also the number of light cone crossings is given.

Tetrahedron	Links	$\cos(\Theta)$	$\sin(\Theta)$	Light cone crossings
T_2	1, 3, 5, 6	$\frac{i}{\sqrt{3}}\sqrt{\frac{\alpha}{4+\alpha}}$	$\frac{2}{\sqrt{3}}\frac{\sqrt{3+\alpha}}{\sqrt{4+\alpha}}$	1
	2	$1+\frac{2\alpha}{3}$	$\frac{2i\sqrt{\alpha(3+\alpha)}}{3}$	0
	4	$\frac{2+\alpha}{4+\alpha}$	$\frac{2\sqrt{3+\alpha}}{4+\alpha}$	N/A
T_3	1	$\frac{i(1+2\alpha)}{\sqrt{3+12\alpha}}$	$2\sqrt{\frac{1+\alpha(4+\alpha)}{3+12\alpha}}$	1
	2, 3	$\frac{2+\alpha}{\sqrt{3}\sqrt{-\alpha(4+\alpha)}}$	$\frac{2}{\sqrt{3}}\sqrt{\frac{1+\alpha(4+\alpha)}{\alpha(4+\alpha)}}$	1
	4, 5	$\frac{1}{\sqrt{17+\frac{4}{\alpha}+4\alpha}}$	$\frac{2}{\sqrt{4+\frac{\alpha}{1+\alpha(4+\alpha)}}}$	N/A
	6	$\frac{2+\alpha(4+\alpha)}{\alpha(4+\alpha)}$	$-\frac{2i\sqrt{1+\alpha(4+\alpha)}}{\alpha(4+\alpha)}$	0
T_5	1, 2, 3	$-\frac{i}{\sqrt{3}\sqrt{1+4\alpha}}$	$\frac{2}{\sqrt{3}}\frac{\sqrt{1+3\alpha}}{\sqrt{1+4\alpha}}$	1
	4, 5, 6	$\frac{1+2\alpha}{1+4\alpha}$	$\frac{2\sqrt{\alpha(1+3\alpha)}}{1+4\alpha}$	N/A
T_9	1, 6	$\frac{3+4\alpha}{1+4\alpha}$	$-\frac{2i\sqrt{2+4\alpha}}{1+4\alpha}$	0
	2, 3, 4, 5	$-\frac{1}{1+4\alpha}$	$\frac{2\sqrt{2}\sqrt{\alpha(1+2\alpha)}}{1+4\alpha}$	N/A

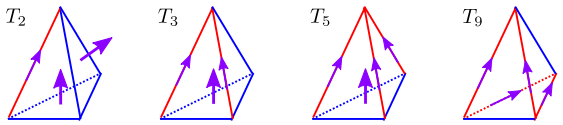

FIG. 12 (color online). The four fundamental tetrahedral building blocks, each equipped with one (out of two possible) time orientations.

rings. In a triangulation with boundary, also open chains are possible.

Using these simplicial substructures, we can construct three-dimensional analogues of the "bubbles" of Sec. III above, by which we will mean connected pieces of triangulation enclosed by a surface made of only spacelike triangles, with no such triangles in its interior. If a ring only contains tetrahedra of type T_2, we get a simple bubble, consisting of two spatial disks with identical structure and a timelike link in its interior [Fig. 13(a)]. By inserting T_3 tetrahedra into a ring of T_2 tetrahedra, we can form more complicated bubbles, as illustrated by Fig. 13(b). More general bubbles consist of an outer ring of T_2 and T_3 tetrahedra, enclosing one or more tetrahedra of the other two types, like the one shown in Fig. 13(c).

We can also consider a ring of T_3 tetrahedra, as depicted in Fig. 13(d). The spacelike triangles marked in yellow form a spatial disk, with a similar spacelike disk just below. Both disks meet in a single vertex, their respective centers, which we will refer to as a *pinching* at that vertex. This situation can be generalized by inserting tetrahedra of type T_2 into the T_3 ring, as shown in Fig. 13(e). The effect is that the two spatial disks now intersect in a link rather than a vertex. Bubbles and pinchings can occur in combination to create even more complicated structures, an example of which is shown in Fig. 13(f). A feature of bubbles which we have not yet mentioned is that they can self-overlap, in the sense that the spherical (or possibly higher-genus) surface bounding a bubble may touch itself along some subset of the surface triangulation. As explained below, we will exclude one kind of self-overlapping bubbles from our simulations, namely, those that wrap nontrivially around the spatial two-sphere.

C. Kinematical constraints

The simplest information one can extract from a triangulation is the number of its subsimplices of a particular type. We will use the following counting variables for the four fundamental tetrahedra and the lower-dimensional subsimplex types, as well as their sums in each dimension:

$$
\begin{aligned}
N_0 &= \text{number of vertices} \\
N_1^s &= \text{number of spacelike links} \\
N_1^t &= \text{number of timelike links} \qquad N_1 := N_1^s + N_1^t \\
N_2^{sss} &= \text{number of triangles with three spacelike links} \\
N_2^{sst} &= \text{number of triangles with two spacelike links} \\
N_2^{tts} &= \text{number of triangles with one spacelike link} \\
N_2 &:= N_2^{sss} + N_2^{sst} + N_2^{tts} \\
N_3^{T_2} &= \text{number of tetrahedra of type } T_2 \\
N_3^{T_3} &= \text{number of tetrahedra of type } T_3 \\
N_3^{T_5} &= \text{number of tetrahedra of type } T_5 \\
N_3^{T_9} &= \text{number of tetrahedra of type } T_9 \\
N_3 &:= N_3^{T_2} + N_3^{T_3} + N_3^{T_5} + N_3^{T_9}. \qquad (3)
\end{aligned}
$$

There exist linear identities among these numbers, which for CDT have been described in Ref. [16]. Here we will repeat the analysis for the extended ensemble, including the new tetrahedral building blocks. The first identity,

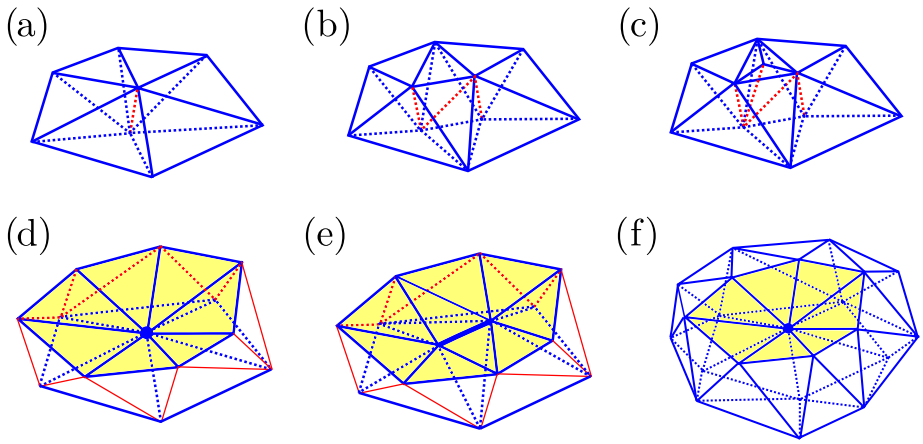

FIG. 13 (color online). (a) A ring of T_2 tetrahedra, forming a simple bubble. (b) By inserting tetrahedra of type T_3, we can form more complicated bubbles. (c) More general bubbles also contain other tetrahedra types. (d) A ring of T_3 tetrahedra gives rise to a pinching, where two spatial disks meet in a single vertex. (e) By adding two T_2 tetrahedra, the pinching is extended to a link. (f) Bubbles and pinchings can occur in combination (timelike links are omitted here).

$$N_0 - N_1 + N_2 - N_3 = \chi, \tag{4}$$

involves the Euler characteristic χ of the simplicial spacetime manifold. Since every tetrahedron contains four triangles and every triangle is shared by two tetrahedra, we also have the constraint

$$N_2 = 2N_3. \tag{5}$$

Both relations (4) and (5) are shared by Euclidean DT and standard CDT. In the latter we also have the foliation constraint $2N_2^{sss} = N_3^{T_5}$, which expresses the fact that in CDT every spacelike triangle is shared by two tetrahedra of type T_5, while every such tetrahedron contains exactly one spacelike triangle. In the present case, the analogous relation is

$$2N_2^{sss} = 2N_3^{T_2} + N_3^{T_3} + N_3^{T_5}. \tag{6}$$

This is easily understood by counting all spacelike faces in the triangulation—the right-hand side of Eq. (6)—and noting that the number of spacelike triangles is half the number of spacelike faces.

In CDT we have two more constraints which explicitly involve the leaves of the preferred foliation. One is the Euler constraint $N_0 - N_1^s + N_2^{sss} = t_{\mathrm{tot}}\tilde{\chi}$, where t_{tot} counts the number of leaves (for periodic boundary conditions in time), and $\tilde{\chi}$ is the Euler characteristic of a spatial section. This constraint no longer exists in the generalized model, since we have Monte Carlo moves which change the quantity $N_0 - N_1^s + N_2^{sss}$. Furthermore, in standard CDT every spacelike triangle has three spacelike links, and every spacelike link is shared by two spacelike triangles, yielding the relation $N_1^s = 3N_2^{sss}/2$. As shown in Ref. [23], this can be generalized to the case at hand, leading to the linear relation

$$N_1^s = \frac{1}{2}(3N_2^{sss} - N_3^{T_2}). \tag{7}$$

Lastly, a constraint which does not have a counterpart in foliated CDT follows directly from our earlier observation of T_2 and T_3 tetrahedra forming closed rings (assuming compact spatial topology), namely,

$$N_2^{sst} = N_3^{T_2} + N_3^{T_3}. \tag{8}$$

We have checked that the Monte Carlo moves for the nonfoliated CDT model, described in Sec. VI below, are not compatible with the existence of other linear relations among the counting variables (3). This means that we have a total of 5 such relations for 10 variables, compared with 5 relations for 7 counting variables for standard CDT quantum gravity in 2 + 1 dimensions. In the next section, we will express the gravitational action as a function of the five remaining independent counting variables.

V. ACTION AND WICK ROTATION

The gravitational path integral (1) assigns to every spacetime geometry $[g]$ a complex amplitude $\exp(iS[g])$, where $S[g]$ is its classical action. As already noted, we will use the same Regge implementation of the Einstein–Hilbert action in 2 + 1 dimensions as previous work on CDT quantum gravity [16], namely,

$$\begin{aligned} S_{\mathrm{Regge}} = {} & k \sum_{\text{spacelike } l} V(l)\frac{1}{i}\Big(2\pi - \sum_{\text{tetrahedra at } l}\Theta\Big) \\ & + k \sum_{\text{timelike } l} V(l)\Big(2\pi - \sum_{\text{tetrahedra at } l}\Theta\Big) \\ & - \lambda \sum_{\text{tetrahedra } T} V(T), \end{aligned} \tag{9}$$

where k and λ are the gravitational and cosmological couplings (up to rescaling), $V(l)$ and $V(T)$ the volumes of a link l and a tetrahedron T, and $\sum\Theta$ denotes the sum over dihedral angles contributed by the tetrahedra sharing a link l. It was shown in Ref. [16] that an analytic continuation $\alpha \mapsto -\alpha$ in the asymmetry parameter through the lower-half complex plane defines a nonperturbative Wick rotation which converts the amplitudes $\exp(iS_{\mathrm{Regge}})$ to real weights $\exp(-S^{\mathrm{eucl}}_{\mathrm{Regge}})$, and thereby makes it possible to analyze the path integral with the help of Monte Carlo simulations. Maintaining the relation $\ell_t^2 = -\alpha\ell_s^2$ between time- and spacelike length assignments, this implies that timelike links acquire a *positive* squared length after the Wick rotation and therefore effectively become spacelike. The requirement that the full set of link lengths corresponds to a proper triangulation *after* the Wick rotation means that they have to obey triangle inequalities, which in turn puts a restriction on the value of α before the Wick rotation, which for CDT in 2 + 1 dimensions takes the form $\alpha > 1/2$.

Let us study how the enlargement of the ensemble of configurations in nonfoliated CDT affects the behavior of the Regge action (9) under the map $\alpha \mapsto -\alpha$. In the first term, $V(l) = 1$ because the link is spacelike. The plane orthogonal to the link has Lorentzian signature. Because we have imposed link causality, we will cross the light cone four times when circling around the link in the plane. According to our complex angle prescription, each crossing adds a real contribution $\pi/2$ to the total dihedral angle, such that the deficit angle—the expression $(2\pi - \sum\Theta)$ inside the parentheses—becomes purely imaginary, like in usual CDT, and under the analytic continuation becomes a real deficit angle.

In the second term, the plane orthogonal to the timelike link is Euclidean and remains so after the Wick rotation. On the other hand, we have $V(l) = \sqrt{\alpha}$, which acquires a factor of $-i$ under the analytic continuation. This implies that the second term changes from real to purely imaginary, as it should. To evaluate the third term, we need the volumes of the tetrahedra, which are shown in Table II. The three-volumes as functions of α are useful quantities

TABLE II. Volumes of the four elementary tetrahedra and conditions on the asymmetry parameter α, which ensure that the building blocks after the Wick rotation are well defined.

Tetrahedron	Volume	Wick rotation condition
T_2	$\frac{1}{12}\sqrt{\alpha(3+\alpha)}$	$0<\alpha<3$
T_3	$\frac{1}{12}\sqrt{1+4\alpha+\alpha^2}$	$2-\sqrt{3}<\alpha<2+\sqrt{3}$
T_5	$\frac{1}{12}\sqrt{1+3\alpha}$	$\frac{1}{3}<\alpha$
T_9	$\frac{1}{6}\sqrt{\frac{1}{2}+\alpha}$	$\frac{1}{2}<\alpha$

to look at. In the Lorentzian sector ($\alpha > 0$), they are all real and positive. After Wick rotation, a vanishing of the volume $V(T)$ signals a geometric degeneracy of the underlying (Euclidean) tetrahedron T, associated with a violation of the triangle inequalities. In addition, note that for the Wick-rotated expressions to give the correct contributions to the Euclidean action, the arguments of the square roots in the second column have to be negative after the substitution α by $-\alpha$, leading to the restrictions on the original α values displayed in the third column of the table. Since all of these constraints have to be satisfied simultaneously, we conclude that in nonfoliated CDT in three dimensions, we need

$$\frac{1}{2} < \alpha < 3 \tag{10}$$

in order for the usual Wick rotation to be well defined, which is stronger than the corresponding condition $1/2 < \alpha$ in CDT, where only the building blocks T_5 and T_9 are used.

Evaluating the Regge action (9) with the help of the expressions in Tables I and II and applying the Wick rotation leads to

$$S^{\text{eucl}} = \tilde{c}_1 N_0 + \tilde{c}_2 N_3 + \tilde{c}_3 N_3^{T_2} + \tilde{c}_4 N_3^{T_3} + \tilde{c}_5 N_3^{T_5} \tag{11}$$

for the Euclideanized Regge action, as a function of a specific linearly independent subset of the counting variables (3), where the explicit functional form of the coefficients $\tilde{c}_i = \tilde{c}_i(k, \lambda, \alpha)$ has been derived in Ref. [23].

For the special case $\alpha = -1$ and after some manipulations using the kinematical constraints, the action (11) can be written as

$$S^{\text{eucl}} = -2k\pi N_1 + \left(\frac{\lambda}{6\sqrt{2}} + 6k \arccos\frac{1}{3}\right) N_3, \tag{12}$$

which coincides with the action of Euclidean dynamically triangulated gravity in three dimensions. We have also checked that by setting $N_3^{T_2} = N_3^{T_3} = 0$, the action (11) can be rewritten to precisely match the Regge action for standard CDT quantum gravity in 2 + 1 dimensions given in Ref. [16].

VI. NUMERICAL SETUP

A. Monte Carlo moves

To set up numerical simulations of nonfoliated CDT quantum gravity in 2 + 1 dimensions, we need to define a set of Monte Carlo moves. In this section, we will present a compact description of the moves, which fall into two groups; further details can be found in Ref. [23]. The first group contains generalizations of the moves that were already used for CDT simulations in 2 + 1 dimensions [16] and which in turn are adapted versions of the original Pachner moves for Euclidean DT [31,32].

Figure 14 shows the three adapted Pachner moves in 2 + 1 dimensions. They all change the interior of a small compact region of the simplicial manifold, while leaving its boundary invariant. For CDT triangulations, once the location of a link to be added has been fixed, its type (timelike or spacelike) is also fixed. This is no longer true in the nonfoliated CDT model, where each of these moves comes in several "flavors." A move of this kind is called am "m-n move" if m and n are the numbers of tetrahedra in the local simplicial neighborhood before and after the move is executed. The 2-6 move is the only generalized Pachner move which creates a new vertex.

The Monte Carlo moves in the second group are new compared to standard CDT. Three of them implement the collapse of a link and only differ in the types of links and the local neighborhood involved, as illustrated by Fig. 15. They can be seen as special cases of the most general link collapse move, of which we currently do not know whether and how it can be implemented efficiently.

The bubble move (Fig. 15, top left) operates on a ring of T_2 tetrahedra with a single timelike link in its interior, forming a bubble according to the definition given in Sec. IV. It collapses the timelike link to a single vertex

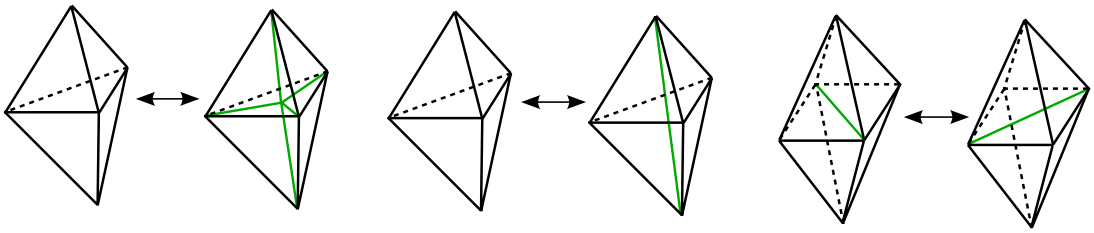

FIG. 14 (color online). The three generalized Pachner moves for CDT in 2 + 1 dimensions: 2-6 move (left), 2-3 move (center), and 4-4 move (right). The links shown in green are removed or created by the corresponding move.

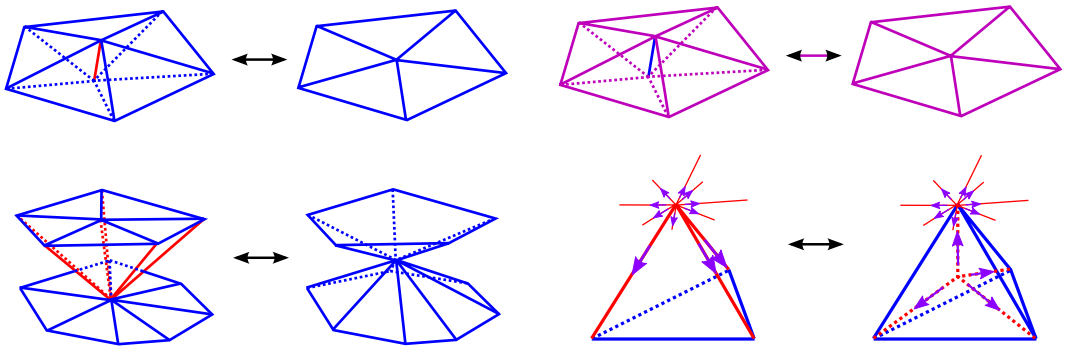

FIG. 15 (color online). New Monte Carlo moves in nonfoliated CDT. Three link collapse moves: bubble move (top left), pinching move (bottom left), and link collapse move for spacelike links (top right). Also shown is the polar move (bottom right), with arrows indicating a time orientation. Spacelike links are blue, timelike ones are red, and purple links (top right) can be either space- or timelike.

and simultaneously collapses the bubble to a spatial disk. The pinching move (Fig. 15, bottom left) operates on a pair of spatial disks whose centers are connected by a timelike link. It collapses this link, leading to a configuration where the disks touch in a single vertex, thereby forming a ''pinching'' as described in Sec. IV [cf. Fig. 13(d)].

We have also implemented a move which collapses a spacelike link (Fig. 15, top right). Note that in the configuration before the collapse, the link types of the upper and lower disk do not necessarily have to match. In the special cases when they do, we call this move *symmetric*. It means that during the collapse, only links of the same type get identified pairwise. To keep the complexity of the implementation at a manageable level, we have restricted ourselves to the symmetric version of this move.

Lastly, recall our introduction in Sec. III of an isolated source and sink of time in $1+1$ dimensions (Fig. 7). We will use a straightforward generalization to $2+1$ dimensions of these local (causality-violating) configurations as our boundary conditions. The polar move operates on the neighborhood of such a source or sink of time, and moves it around. Figure 15 (bottom, right) illustrates the situation for a time source, initially located at the top of the single tetrahedron on the left. The move subdivides the tetrahedron into four, with the newly created vertex at the center becoming the new source of time.

An important feature of a set of Monte Carlo moves is that it should be ergodic; that is, any element of the configuration space can be reached in a finite number of moves. In our case, the configuration space $\tilde{\mathcal{C}}$ consists of all locally causal gluings of the elementary building blocks T_2, T_3, T_5, and T_9 that can be time oriented consistently and satisfy further regularity conditions specified in the next subsection. We have made the standard choice of a direct product $[0,1]\times S^2$ for the spacetime topology. It is possible that the moves described here are ergodic in this configuration space; in fact, the original motivation for introducing additional building blocks was to let us move around in the space of triangulations more efficiently. However, we do not have a proof of ergodicity and suspect this could be rather nontrivial, given the nonlocal character of part of the causality conditions.

B. Defining the ensemble

As already mentioned in Sec. II, previous simulations of CDT in $2+1$ dimensions have worked with a fixed spacetime topology of direct-product form $[0,1]\times {}^{(2)}\Sigma$, or $S^1\times{}^{(2)}\Sigma$ if time is compactified. The standard, simplest choice[8] for the spatial topology—which we will also employ in the present work—is the sphere, ${}^{(2)}\Sigma = S^2$. *A posteriori*, the choice of compactifying time in this case does not appear to make much of a difference because it turns out that the *dynamics* of $2+1$ CDT quantum gravity (for sufficiently large time extension t_{tot} of the configurations) drives the shape of the universe toward a de Sitter space with S^3 topology [18].

As we will now go on to explain, the most convenient choice of boundary conditions for nonfoliated CDT is that of a direct-product spacetime $[0,1]\times S^2$, where the beginning and end of time are allowed to degenerate to a point, leading effectively to an S^3 topology. Recall that in simulations of CDT quantum gravity, the number of time steps t_{tot} is fixed. Since genuine foliated CDT triangulations form a subset of the present ensemble $\tilde{\mathcal{C}}$, the question arises whether it is possible to go from one strictly foliated configuration to another one with a different number t'_{tot} of time steps via nonfoliated configurations and using the Monte Carlo moves described in the last subsection. As explained in detail in Ref. [23], the answer is yes. It follows that if there is a region in the phase diagram where the configurations are close to foliated, the standard CDT notion of the ''number of time steps'' will also make sense approximately, and one can ask which equilibrium value for this quantity is found after thermalization. During early test simulations in the ensemble $\tilde{\mathcal{C}}$ with compactified time, we did find configurations that were approximately foliated, but the number of time steps would not thermalize

[8]For a recent investigation with toroidal slices, see Ref. [33].

properly. We have been able to circumvent this problem by not compactifying time and adding a source and a sink of time as the two poles of a three-sphere.

Another technical issue which appeared during early test runs was that the simulations would often end up in "frozen" states where virtually no progress could be made using the implemented Monte Carlo moves. The problem could be traced back to the presence of globally self-overlapping bubbles, winding once or multiple times around the spatial sphere (cf. our discussion in Sec. IV). Since we were unable to overcome this problem by finding additional moves, we looked for a mechanism to prevent the globally self-overlapping bubbles from appearing. We found that these problematic structures do not form when we forbid all moves which merge or split bubbles. The moves of Fig. 15 are essentially unaffected by these restrictions (see Ref. [23] for details). The simulations on the reduced ensemble behaved much better after this alteration, although there are still phase space regions where they do not thermalize sufficiently well, as we will discuss later.

Finally, we will use local regularity conditions for the gluings that make the triangulations into simplicial manifolds, which means that each (interior) vertex has a ball-like neighborhood whose surface is a triangulated two-sphere. This is the choice made in most of the work on higher-dimensional CDT quantum gravity and will allow for a better comparison of results.

C. Reintroducing time

The distribution of spatial volume as a function of time is an important large-scale observable, and its analysis has been instrumental in relating CDT quantum gravity to a de Sitter minisuperspace cosmology in $2+1$ and $3+1$ dimensions [10,18]. In order to perform a similar analysis also in nonfoliated CDT, we need to define a time coordinate on its generalized configurations. As explained in the introduction, the fact that spatial slices will generally branch and form bubbles means that we can no longer use them to define a distinguished time variable.

To explain our alternative prescription of "time," consider a time-oriented member of the configuration space $\tilde{\mathcal{C}}$. Given a vertex V, consider the set of all future-oriented paths connecting V with the north pole. The number of links in each path defines a distance between V and the north pole. By averaging this quantity over all paths, we obtain an average distance d_f. Repeating the procedure for past-oriented paths, connecting v to the south pole, gives another average distance d_p. The time coordinate of V is then defined as $t = d_f - d_p$. Note that for foliated CDT configurations, this coincides with the usual discrete proper time, up to a trivial factor. We have experimented with other notions of time, including that of shortest distance to the poles; they generally lead to a "washing out" of the tetrahedron distributions described below. It is possible that alternative notions of time are more appropriate or practical for observables different from the ones studied here.

Since the number of oriented paths between a vertex and a pole can become very large, in practice we used a modified algorithm, which calculates t in an approximate fashion. For each vertex we constructed a fixed number of future-oriented paths, using a random process which jumps iteratively from a vertex to a randomly chosen future neighbor until the north pole is reached. We then repeated this process for past-oriented paths and finally calculated the time coordinate as the difference of both average distances.

Given this new notion of time, we can now also assign an (average) time to spatial slices. We define a *spatial slice* in nonfoliated CDT—with boundary conditions as specified above—as any subset of spatial triangles forming a two-sphere, such that by cutting along the sphere, the spacetime triangulation decomposes into two disconnected parts, with time flowing consistently from one side of the cut to the other. In other words, the future-pointing arrows introduced in Fig. 12 are all lined up to point in the same direction away from the slice. The time coordinate we assign to such a slice is the average of all time coordinates of its vertices. Note that unlike in standard CDT, where different spatial slices are always disjoint, spatial slices here can have any amount of overlap.

We now have all the ingredients to measure the desired volume profiles. Since the number of spatial slices of an individual path integral configuration can become very large, we use a statistical method to generate a subset of spatial slices which is evenly distributed along the time direction. In order to perform an ensemble average of the volume distribution, we use a nontrivial averaging algorithm, the details of which are described in Ref. [23].

VII. EXPLORING THE PHASE DIAGRAM

We have developed the necessary Monte Carlo simulation software, using C++ as programming language and taking advantage of object-oriented design principles to incorporate modularity and flexibility into the software. We had anticipated that the software would be more complex than for the CDT simulations but in the event its complexity even surpassed our expectations. An extended discussion of the details of the software implementation, with special emphasis on the Monte Carlo moves, is given in Ref. [23]. In what follows, we will present the results obtained with the simulation software, beginning with an exploration of the phase diagram of nonfoliated CDT quantum gravity in $2+1$ dimensions.

The Regge form (9) of the gravitational action contains two couplings, k and λ, which are proportional to the inverse bare Newton's constant and the bare cosmological constant, respectively. When evaluating the action on causal triangulations, a third parameter—the asymmetry α—naturally appears because of the distinction between space- and timelike links. Together they span a three-dimensional space of

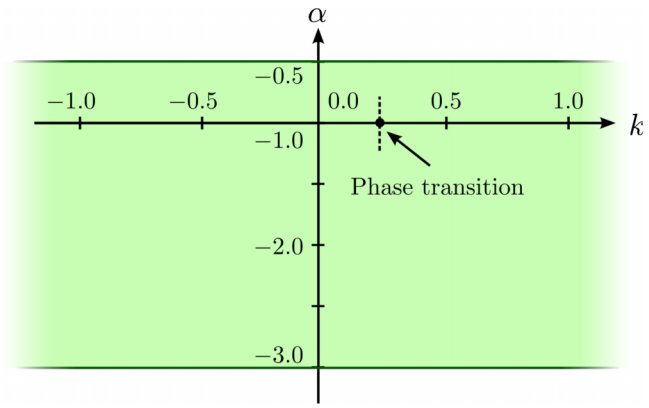

FIG. 16 (color online). The phase diagram of nonfoliated CDT quantum gravity is the region inside the strip $-3 < \alpha < -1/2$, visualized in green. Our investigation has probed the phase space along the two axes drawn in the figure: at various k values for constant $\alpha = -1$ and at various α values for constant $k = 0$.

bare actions. Of course, from the way α is introduced in the regularized theory, there is no *a priori* reason why it should play the role of a coupling constant. Different α values should lead to the same continuum gravity theory. This expectation is consistent with the dynamical results found below.[9]

As usual in dynamically triangulated systems, we do simulations at fixed system size N_3 and then perform a finite-size scaling analysis to extrapolate to the limit of infinite size. This means that the phase diagram of the model is spanned by the parameters k and α. As we have derived in Sec. V, the existence of a Wick rotation limits the allowed values for α to the region $1/2 < \alpha < 3$. Sticking with the notation "α" for this parameter also after the analytic continuation, the Wick rotation maps this region to the range $-3 < \alpha < -1/2$. The phase diagram of our generalized CDT model is therefore a strip bounded by these two α values, as illustrated by Fig. 16.

In the following we will analyze the dynamics of our model at a range of points along the two axes drawn in the figure. While the simulations work well on the axis defined by constant $\alpha = -1$, we encountered difficulties when exploring the axis of constant $k = 0$ in the region $-3 < \alpha < -1$. As one moves away from $\alpha = -1$ toward $\alpha = -3$, the number of accepted Monte Carlo moves goes down significantly, and the thermalization time increases rapidly. A closer analysis revealed that the severity of the problems correlates with the presence of bubbles with a complicated internal structure. These problems imply that we currently must concentrate our investigation on the region $-1 < \alpha < -1/2$.

A. Bounds on the vertex density

In $2 + 1$ dimensions there are kinematical bounds on the ratios of certain counting variables, like the vertex density N_0/N_3 and the link density N_1/N_3. In the case of CDT, the link density satisfies $1 \leq N_1/N_3 \leq 5/4$ [16], which should be compared with the weaker bound $1 \leq N_1/N_3 \leq 4/3$ for DT. Using the linear relations (4) and (5), one easily derives $N_0/N_3 = N_1/N_3 - 1$ in the infinite-volume limit, which means that we can translate the link density bounds into the vertex density bounds $0 \leq N_0/N_3 \leq 1/4$ for CDT and $0 \leq N_0/N_3 \leq 1/3$ for Euclidean triangulations.

The derivation of the link density bound in CDT involves the spatial Euler constraint, which is not present in the ensemble $\tilde{C}$ we have specified in Sec. VI above. To find the analogous bound for nonfoliated CDT configurations, we follow Ref. [16] in considering all Monte Carlo moves that create a vertex. Since all of them change the number of tetrahedra by some amount ΔN_3, the strategy is to select those moves for which ΔN_3 is minimal. Starting with a minimal triangulation and repeatedly applying only the selected moves, the vertex density and thus also the link density will be maximized, and the corresponding bounds follow upon taking the infinite-volume limit.

In the case at hand, we have two Monte Carlo moves which create one vertex and three tetrahedra, namely, the bubble move and the polar move described in Sec. VI above. Both are unconstrained moves which can always be executed. We conclude that in nonfoliated CDT quantum gravity, the vertex and link densities satisfy the bounds

$$0 \leq \frac{N_0}{N_3} \leq \frac{1}{3} \quad \text{and} \quad 1 \leq \frac{N_1}{N_3} \leq \frac{4}{3}. \tag{13}$$

These relations agree with those for Euclidean DT, but the configurations which saturate them differ substantially, as we will see. Note that a relaxation (in the sense of Ref. [34]) of the local regularity conditions for a simplicial manifold would weaken these bounds, since then bubbles with fewer than three tetrahedra can occur.

Figure 17 shows the measurements of the average vertex densities for various values of the coupling k, from simulations with $\alpha = -1$ and system size $N_3 = 40.000$. The vertex density increases monotonically with k, which is not surprising since (at fixed N_3) larger values of k favor the creation of vertices. This can be seen easily by rewriting Eq. (12) with the help of the kinematical constraints, yielding $S^{\text{eucl}} = -2k\pi N_0$ plus a term proportional to N_3. As expected, the measured curve in Fig. 17 approaches the upper kinematical bound of $1/3$ for large values of k. We also see a clear signal of a phase transition between $k = 0.24$ and $k = 0.28$, from a phase of low to one of high vertex density, reminiscent of the first-order transitions in the inverse gravitational coupling found in both DT [35] and CDT [18]. Analogous measurements for fixed $k = 0$ and varying α show that the vertex densities are approximately constant at low values, without any sign of a phase transition. Of course, since we are only investigating the region $-1 < \alpha < -1/2$ of the phase diagram, we cannot

[9] In $3 + 1$ dimensions the status of the analogous parameter α is more involved [8,11].

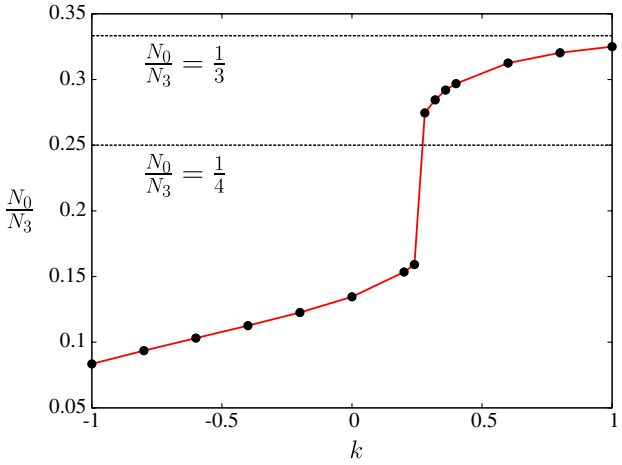

FIG. 17 (color online). Measurement of the average vertex density N_0/N_3 as a function of the inverse gravitational coupling k, for $\alpha = -1$ and system size $N_3 = 40.000$. The dots represent actual measurements and the lines linear interpolations. The dashed lines mark the kinematical bounds for standard DT (upper line) and CDT (lower line).

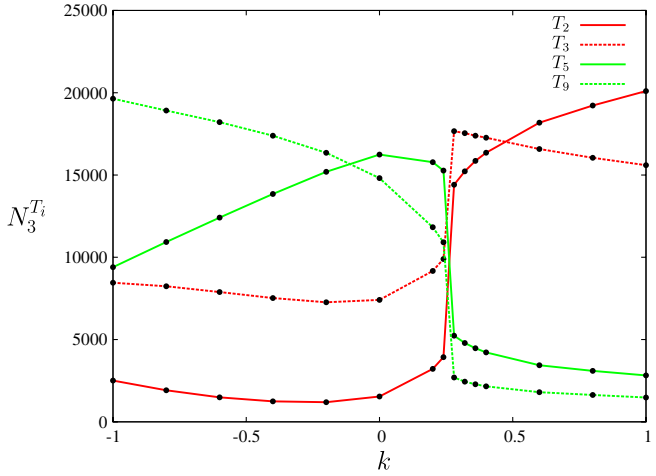

FIG. 18 (color online). The numbers of tetrahedra of each of the four types, averaged over the sampled triangulations, as function of the coupling k, at $\alpha = -1$ and $N_3 = 40.000$.

exclude the presence of further phase transitions in the complementary region.

B. Emergence of foliated triangulations

Foliated CDT geometries form a subset of the ensemble $\tilde{\mathcal{C}}$, characterized by the condition $N_3^{T_2} = N_3^{T_3} = 0$.[10] By plotting the number of tetrahedra of these two types as

[10]With periodic boundary conditions in time, one could in principle construct a triangulation obeying $N_3^{T_2} = N_3^{T_3} = 0$ consisting of a single bubble winding around both space and time, which clearly is not foliated. However, such configurations do not lie in $\tilde{\mathcal{C}}$ because in our case, time is not compactified, and we do not allow for globally self-overlapping bubbles.

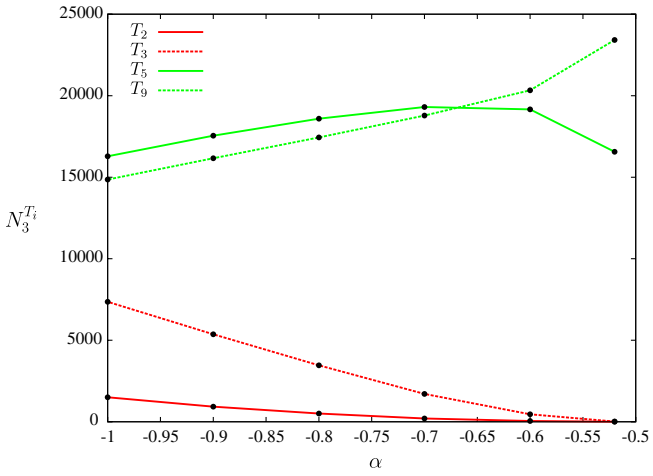

FIG. 19 (color online). The numbers of tetrahedra of each of the four types, averaged over the sampled triangulations, as a function of the coupling α, at $k = 0$ and $N_3 = 40.000$.

function of the couplings, we can therefore look for regions in phase space where foliated triangulations emerge dynamically. Figure 18 shows the numbers of all tetrahedral types used, averaged over the configurations sampled from $\tilde{\mathcal{C}}$, as a function of the coupling constant k. In the phase with low vertex density on the left, although the building blocks of standard CDT dominate, also the other two types appear in significant numbers, from which we deduce that the triangulations along the line $\alpha = -1$ apparently are not foliated.

Conversely, Fig. 19 shows the expectation values of the numbers of tetrahedra at fixed $k = 0$, as function of α. Note that the phase boundary $\alpha = -0.5$ does not belong to the phase diagram, since the Wick rotation is not defined there. The measurements corresponding to the rightmost data points in the figure have been performed at $\alpha = -0.52$. We find that both $N_3^{T_2}$ and $N_3^{T_3}$ approach zero as we move toward the phase boundary. At $\alpha = -0.52$ we have measured $\langle N_3^{T_2} \rangle \approx 2.9$ and $\langle N_3^{T_3} \rangle \approx 14.3$, which means that in the entire system consisting of 40.000 tetrahedra, almost none of the building blocks belong to the new types T_2 and T_3.

We conclude that the configurations appearing close to $\alpha = -0.5$ are almost perfectly foliated and belong to the phase with low vertex density. Effectively, the dynamics should therefore be very close to the known dynamics of 2 + 1-dimensional CDT in the extended phase [18], and we would expect the geometries to be macroscopically extended with a characteristic blob-shaped volume distribution. These expectations will be confirmed later on.

VIII. TETRAHEDRON DISTRIBUTIONS

We have seen in the last section that foliated configurations emerge close to the boundary of the phase diagram. As we move away from the boundary, the configurations

become less foliated. A strict foliation is attained whenever $N_3^{T_2} = N_3^{T_3} = 0$, but it is unclear how to translate nonzero values into a measure of foliatedness of a triangulation. We would like to have a more refined observable which tells us how foliated a triangulation is. In the following we will use tetrahedron distributions based on the time coordinate introduced in Sec. VI as a qualitative tool to investigate the degree of foliatedness of a triangulation.

To start with, let us assume that all vertices have been assigned a time coordinate using the algorithm described in Sec. VI. For each tetrahedron we then calculate the sum of the time coordinates of its four vertices and round this value to the nearest integer. By definition, this value gets assigned to the tetrahedron as its new time coordinate. This tetrahedron time clearly has a different relative normalization compared to the "vertex time" from which it was derived, but this does not matter as long as we do not use both time coordinates simultaneously.

In a given configuration, we can now count the number of tetrahedra that share the same value of (tetrahedron) time and plot these numbers as a function of time to generate a tetrahedron distribution. Figure 20 (left) shows such a distribution for a strictly foliated CDT geometry, which we have generated by running our simulation with foliation constraint enabled. We observe that the distribution appears as a superposition of two blob-shaped distributions. One can show that one of them consists of T_5 tetrahedra and the other one of T_9 tetrahedra [18]. An enlarged version of the central part of the distribution is shown in Fig. 20 (right), which illustrates that the peaks are organized in groups of three. One can show that every such group corresponds to a "thick slice," which is the triangulation enclosed between two adjacent simplicial spatial hypermanifolds [23], the higher-dimensional analogue of a "strip" in $1 + 1$ dimensions. Note that for pure CDT configurations, the tetrahedron time is effectively a refinement of the number of time steps associated with the preferred foliation, similar to what was considered in Ref. [36] to produce finer-grained volume distributions in $3 + 1$ dimensions.

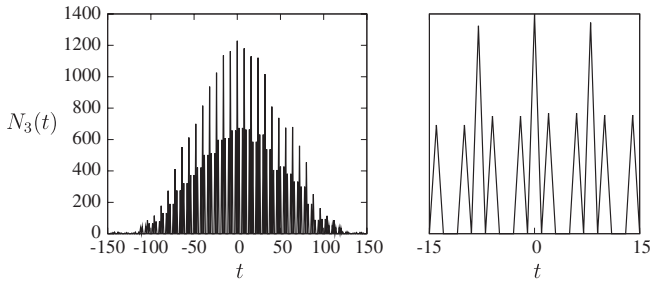

FIG. 20. Typical tetrahedron distribution of a strictly foliated CDT configuration as function of "tetrahedron time," extracted from a simulation with foliation constraint enabled (left). Zooming in on the central region of the distribution, one obtains the graph shown on the right.

Let us return to the more general setting of nonfoliated CDT quantum gravity and focus on triangulations which are a little further away from the phase boundary. Figure 21 shows the tetrahedron distribution of a single triangulation extracted from a simulation at $k = 0$, $\alpha = -0.7$, with volume $N_3 = 40.000$. We observe a sequence of peaks, with some remnants of the three-peak structure exhibited by Fig. 20. The tendency of these structures to become blurred most likely depends both on changes in the actual triangulation and on the precise algorithm used to define the time coordinate and the tetrahedron distribution. Consequently, the relevant information lies not so much in the precise structure of the peaks but in the overall pattern formed by the succession of all the peaks. Comparison of the two configurations suggests that every peak in Fig. 21 corresponds to a group of three peaks in Fig. 20 and describes a structure which resembles a thick slice in a foliated triangulation. Another aspect in which the two configurations differ is the fact that the gaps between each group of three peaks in Fig. 20 (right)—marking the location of spatial triangulated hypermanifolds—are getting filled in when the foliation is relaxed. This can be interpreted as a "decoration" of the spatial slices by the creation of bubbles.

Based on these findings, we can interpret the pattern shown in Fig. 21 as a triangulation where decorated spatial slices alternate with modified thick slices. A triangulation exhibiting such a structure will be called *weakly foliated*. This is obviously not a sharp definition since we are not providing a sharp criterion for when a weakly foliated triangulation changes into a truly nonfoliated one. We will take an operational point of view here and consider a triangulation to be weakly foliated whenever the tetrahedron distribution shows the characteristic alternating pattern.

The next important step is to understand how the foliatedness of a triangulation changes as one moves around in

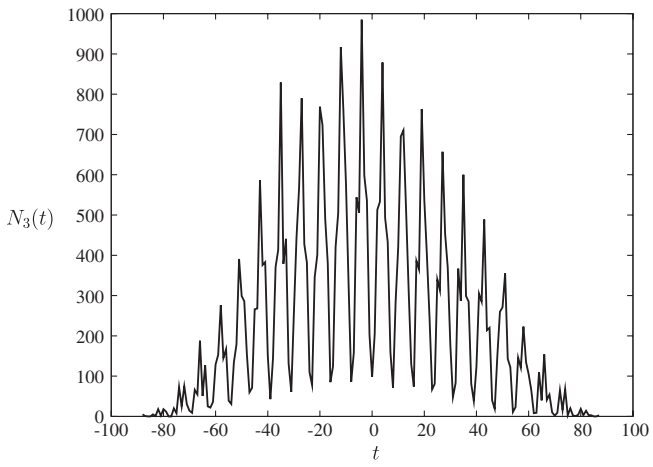

FIG. 21. Tetrahedron distribution of a typical path integral history from a simulation of the generalized CDT model at $k = 0.0$, $\alpha = -0.7$.

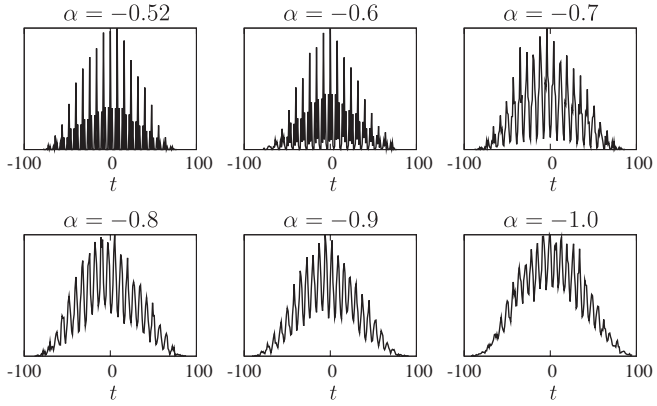

FIG. 22. Tetrahedron distributions of typical path integral configurations from simulations at coupling $k = 0.0$ and system size $N_3 = 40.000$, for various choices of the asymmetry parameter α. Note that all geometries display some degree of being weakly foliated, which becomes weaker with increasing $|\alpha|$.

phase space. Figure 22 shows a sequence of typical tetrahedron distributions of single triangulations extracted from simulations at $k = 0$, for various choices of α. From an almost strict foliation at $\alpha = -0.52$, the signal—although remaining distinctly visible—gradually weakens as we move toward $\alpha = -1$. It would be interesting to follow the development of this pattern beyond this point toward the other phase boundary, but technical issues currently prevent us from doing so, as we have discussed earlier. We have performed a similar analysis on the line of constant $\alpha = -1$ and have observed that the alternating pattern remains visible but becomes less pronounced when one moves from $k = 0$ toward $k = -1$, indicating a further weakening of the foliation. When going from $k = 0$ in the other direction toward the phase transition, the data quality decreases significantly, to such an extent that an interpretation based on the tetrahedron distribution becomes unreliable. To summarize, it appears that all investigated configurations in the phase of low vertex density exhibit some kind of (weak) foliation, whose degree varies significantly, from an almost strict foliation near the phase boundary at $(k, \alpha) = (0, -0.5)$ to a much less pronounced one for larger $|\alpha|$.

IX. VOLUME DISTRIBUTIONS

A. Phase of extended geometry

In Sec. VI we introduced the notions of *time* and spatial slices for a general, nonfoliated CDT geometry. The presence of these ingredients allows us to measure volume distributions—also called *volume profiles*—just like in standard CDT quantum gravity. In the following we will present the results of our numerical investigations. Figure 23 shows the expectation value of the measured volume distributions for various values of the coupling k, for fixed $\alpha = -1$. In all cases the average geometry is macroscopically extended, and the average volume profile has a characteristic blob shape, strongly reminiscent of what is found in CDT in the physically interesting phase [18]. We will report later in this section on a quantitative analysis of the average volume distributions.

Figure 23 illustrates that with increasing k, the time extension of the average geometry also increases. In addition, as one approaches the phase transition, the emergent geometry develops a "tail" at both ends of the volume profile, by which we mean a region of small, approximately constant spatial volume. Since this structure is not resolved in Fig. 23, we have replotted the distributions close to the phase transition (at $k = 0$, 0.2, 0.24) in Fig. 24, with an enlarged scale for the time axis and a small upward shift of the distribution curves. This tail looks similar to the stalk observed in simulations of CDT but is not necessarily related because of the different

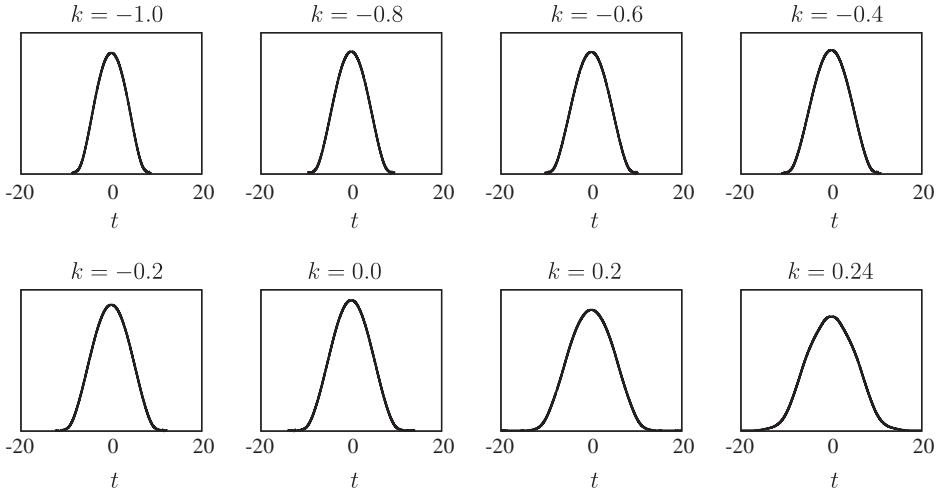

FIG. 23. Average volume profile $\langle N_2(t) \rangle$ as function of time t, measured at $\alpha = -1$ for various values of k. The scale of the vertical axis is the same for all plots. Some of the profiles have a tail which is not visible here but is shown in Fig. 24 below.

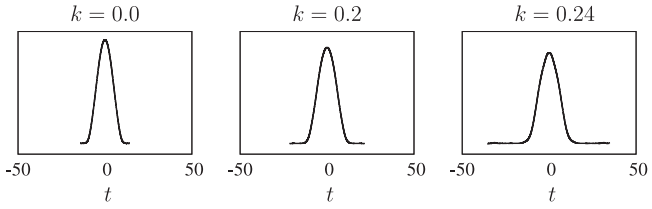

FIG. 24. The last three average volume profiles from Fig. 23, with a different scaling of the time axis and a small upward shift away from the axis to exhibit the tails of the distributions.

choices of boundary conditions. In CDT its presence is enforced by the fact that the simulations are run at a fixed total time extent (equal to the number of spatial slices in the foliation), *and* that the two-volume is not allowed to vanish, but is bounded below by a minimum of four triangles, set by the manifold conditions. In the present case, we employ the same regularity condition, but the time extension of the geometry is dynamical, and the stalk develops spontaneously as we move from $k = 0$ toward the phase transition. Anticipating our interpretation below of the volume profiles in terms of de Sitter universes, the appearance of the tails could be related to quantum corrections to the underlying effective minisuperspace action near the phase transition.

Consider now a volume distribution on the line $\alpha = -1$ *beyond* the transition, that is, in the phase of high vertex density. Figure 25 shows a volume distribution of a typical path integral configuration from a simulation at $(k, \alpha) = (0.4, -1)$ with 40.000 tetrahedra. The qualitative picture in this phase is completely different: the vast majority of spatial slices have (almost) minimal size $N_2(t)$, and the triangulation forms a very long stalk with minimal spatial extent almost everywhere. At this phase space point, we have checked that the time extension of the stalk scales linearly with the system size. In the infinite-volume limit, it

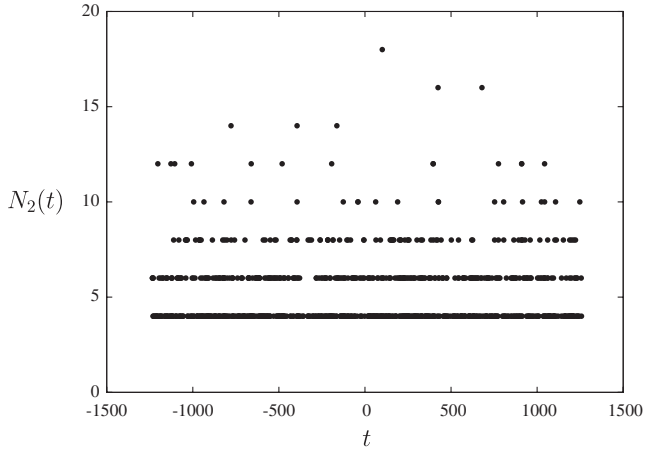

FIG. 25. Volume distribution $N_2(t)$ of a typical triangulation from a simulation at $(k, \alpha) = (0.4, -1)$ and $N_3 = 40.000$ in the phase of high vertex density. The plot shows individual measurement points.

would therefore appear that the "universe" becomes a one-dimensional timelike string.

We can now summarize our findings. At all phase space points investigated, we have found average geometries which are macroscopically extended and whose volume profile has a characteristic bloblike shape. The time extension of the average geometry increases with increasing k, and near the phase transition, the geometry starts to develop tails. On the other side of the transition, the geometries degenerate into long tubes, unrelated to any $2 + 1$-dimensional classical geometry.

B. Evidence for three dimensionality from finite-size scaling

We will investigate next whether we can assign a macroscopic dimensionality to the extended structure of the volume profiles found in the phase of low vertex density by performing a systematic finite-size scaling analysis. To this end, we have run another extended series of simulations, taking data at six points along the axis of constant $\alpha = -1$, ranging from $k = -1.0$ to $k = 0.0$, and at six points along the axis of constant $k = 0$, ranging from $\alpha = -0.52$ to $\alpha = -1.0$. At each point we have performed four simulations with different system sizes, namely, $N_3 = 40$, 80, 120, and $160k$.

Figure 26 (left) shows the measurements of the expectation value of the volume distributions for the four different system sizes at $(k, \alpha) = (0.0, -1.0)$. Following the strategy of Ref. [10] for foliated CDT triangulations in $3 + 1$ dimensions, we will use finite-size scaling to achieve a best overlap of these curves. Assuming that the average geometry has macroscopic dimension d, we expect time intervals to scale like $N_3^{1/d}$ and spatial volumes like $N_3^{(d-1)/d}$. When plotting the distributions with axes rescaled accordingly, the measured curves should fall on top of each other.

To find an estimate for d, we have run an algorithm that scans through an interval of d values in steps of $\Delta d = 0.005$, which for each d value measures how well

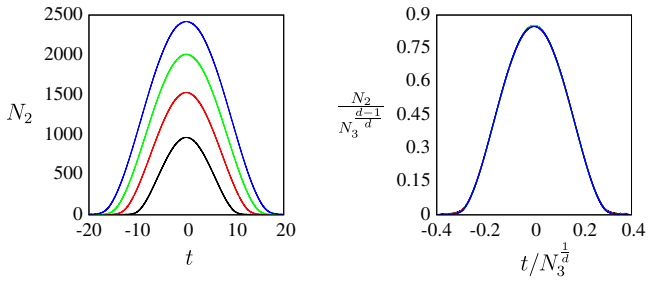

FIG. 26 (color online). Average volume profiles at $(k, \alpha) = (0.0, -1.0)$ for four different system sizes $N_3 = 40$, 80, 120 and $160k$, before (left) and after (right) rescaling the axes as indicated, with $d = 2.91$ to achieve a best overlap, which is seen to be of excellent quality.

the volume profiles overlap. We have employed a standard least-squares measure with appropriate normalization to quantify the quality of the overlap. The value of d which minimizes this measure is taken as an estimate for the macroscopic dimension. For the case at hand, the algorithm yields a best estimate of $d = 2.91$. The plot in Fig. 26 (right) shows all four distributions with axes rescaled using this value for the dimension, resulting in a virtually perfect overlap.

We have repeated the same analysis for the other points in the phase diagram. Figure 27 summarizes the calculated estimates for the macroscopic dimension d, for fixed $\alpha = -1$ (left) and fixed $k = 0$ (right). The large dots indicate measurements with an overlap of excellent quality and the small dots those of a somewhat lesser quality. We observe that all six high-quality measurements yield macroscopic dimensions between $d = 2.85$ and $d = 3.00$, while the values from the remaining six measurements have a larger spread.

We have not included error bars in the plots of Fig. 27 and the values obtained for the dimension d because they are dominated by systematic errors we currently cannot estimate, one possible source being algorithmic dependencies. The calculation of the dimension observable is highly nontrivial and involves several algorithmic choices which potentially affect the final result. Recall that we first had to define a time coordinate, which we did by calculating the average distance between a vertex and the poles of the three-sphere. Second, we assigned a time coordinate to the spatial slices by averaging over the time coordinates of the vertices in the slice. Finally, we ran a rather sophisticated averaging algorithm to produce the final distributions. The nonuniqueness of this entire process is likely to lead to systematic errors not captured by standard error algorithms such as the bootstrap method.

It is clear from this discussion that a single dimension measurement does not provide sufficient evidence to support the $d = 3$ hypothesis, which would imply compatibility with the standard CDT result. On the other hand, all twelve results together suggest strongly that

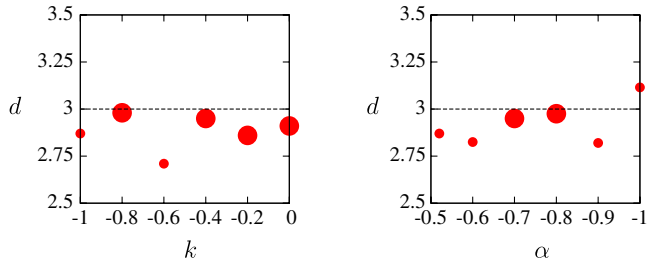

FIG. 27 (color online). Estimates for the macroscopic dimension d from finite-size scaling, from measurements at fixed $\alpha = -1.0$ (left plot) and fixed $k = 0.0$ (right plot). Large dots represent measurements where the volume profiles overlap with excellent quality; the smaller dots stand for overlaps of lesser quality.

the average geometries in the phase of low vertex density are three dimensional. The results on the functional form of the volume profiles presented below will strengthen this preliminary conclusion even further.

C. Comparison with the three-sphere

A crucial piece of evidence that CDT quantum gravity has a well-defined classical limit comes from matching the average distributions of spatial volumes with those of a Wick-rotated version of a solution to the classical Einstein equations, namely, a de Sitter universe [10]. More specifically, the distributions coming from the simulations have been compared to a volume profile of the form $V_3(t) = a\cos^3(bt)$, where t is by assumption proportional to proper time. This is the volume profile of Euclidean de Sitter space (equivalently, the round four-sphere), where the two free parameters a and b depend on the overall size of the universe and a finite relative scaling between spacelike and timelike directions. The measured volume profiles in 3 + 1-dimensional CDT can be fitted with high accuracy to the analytical $\cos^3$ expression [10,36], with the exception of the region very close to the end points of the curve, which cannot be resolved with sufficient precision and is obscured by the regularity condition $\langle N_2(t)\rangle \geq 4$, as we have discussed earlier.

We will perform an analogous analysis of nonfoliated CDT in 2 + 1 dimensions, using the average volume distributions from our simulations. The volume profile of the corresponding continuum de Sitter universe in three dimensions has the functional form $V_2(t) = a\cos^2(bt)$, where a and b are constants. To extract an optimal fit to this two-parameter family of curves from our Monte Carlo data, we have selected only those points in the phase diagram where the rescaled average volume profiles overlap with excellent quality and where we have a well-defined curve to compare to.

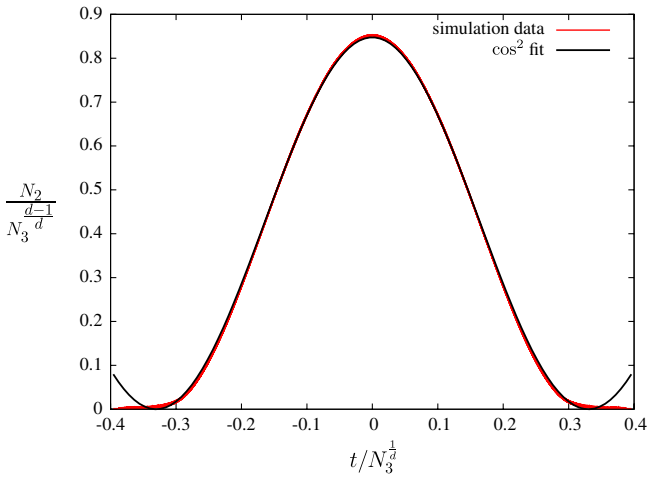

FIG. 28 (color online). Rescaled average volume profiles at $(k, \alpha) = (0.0, -1.0)$, corresponding to dimension $d = 2.91$ and best fit to the $\cos^2$ ansatz.

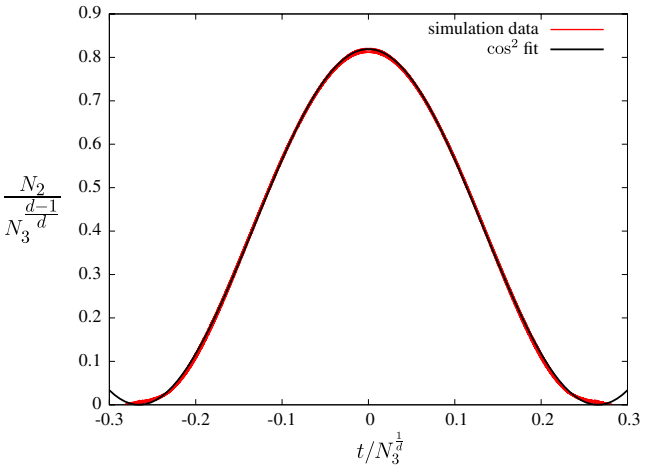

FIG. 29 (color online). Rescaled average volume profiles at $(k, \alpha) = (-0.8, -1.0)$, corresponding to dimension $d = 2.98$ and best fit to the $\cos^2$ ansatz.

Figure 28 shows the outcome of this comparison at the point $(k, \alpha) = (0.0, -1.0)$. Obviously, the only relevant part of the fit function is the region between the two zeros of the $\cos^2$ function. We see that the functional ansatz fits the average volume distributions almost perfectly, except at the two ends, where the simulation data show a small tail which is not present in the fit function once we cut away the parts outside the two minima. We have already commented earlier on the appearance of such tails in the vicinity of the phase transition (see also Fig. 24); in the context of the de Sitter interpretation of our universe, they indeed seem to be related to small-scale deviations from the classically expected result.

From this point of view, it is interesting to understand how the situation changes when one repeats the comparison at a point further away from the phase transition. Figure 29 shows the result of the same analysis performed at the point $(k, \alpha) = (-0.8, -1.0)$. We again observe an almost perfect fit in the region where the spatial volume $N_2(t)$ is nonminimal. Remarkably, now even the total time extension of the dynamically generated universe and the de Sitter fit function between the two minima agrees, and we get an almost perfect semiclassical matching. The quality of the fit becomes slightly reduced toward both ends, which is not surprising because discretization effects become large when the spatial volumes become small.

X. SUMMARY AND CONCLUSIONS

We begun our investigation with the aim to isolate and understand the role of the preferred time slicing in standard CDT quantum gravity, while maintaining causality of the individual path integral histories. In this article we have presented many details of the kinematical and dynamical properties of the new, nonfoliated CDT model in $2 + 1$ dimensions, which implements the dissociation of the causal structure and the preferred notion of time. Due to the presence of new elementary building blocks, the foliation in terms of equally spaced triangulated spatial hypermanifolds is broken up in this extended version of CDT, acquiring novel simplicial substructures such as bubbles and pinchings.

Gravitational dynamics in the new model is implemented in terms of the standard Regge action, defined as a linear function on the space of independent counting variables, which is five-dimensional, compared to CDT's two dimensions. After fixing the total system size, there are two coupling constants spanning the phase space of the model, the bare inverse Newton coupling k and the coupling α, which quantifies the anisotropy between space- and timelike length assignments in the regularized theory. This asymmetry parameter has to satisfy the inequalities $1/2 < |\alpha| < 3$ for the Wick rotation to exist, which is necessary to be able to probe the nonperturbative properties of the model with the help of Monte Carlo simulations. This introduces two boundaries in the phase diagram.

The presence of thermalization problems, preventing the effective implementation of the Monte Carlo algorithm, led us to eliminate certain global simplicial substructures. This allowed us to investigate the region $-1 \lesssim \alpha < -1/2$ of the phase diagram (in terms of the analytically continued α), while we still observed severe thermalization problems in the complementary region. We ran the simulations with the spacetime topology of a three-sphere with a source and a sink of (Euclidean) time at the two poles.

In terms of results, we have found two phases of geometry with low and high vertex density, for k values below and above some critical value k_c of the inverse gravitational coupling, respectively. The analysis of the tetrahedron distributions revealed that the triangulations remain weakly foliated throughout the investigated phase space region of low vertex density but that the strength of this signal varies significantly as a function of the bare couplings. In addition, we observed the emergence of almost perfectly foliated simplicial geometries close to the boundary $\alpha = -1/2$ of the phase diagram. We constructed a volume distribution observable and an averaging procedure to study the expectation value of the volume profiles of the emergent geometries in the weakly foliated phase. A finite-size scaling analysis provided strong evidence that the extended geometries are macroscopically three dimensional. Additional support for this came from fitting the measured profiles to a $\cos^2$ ansatz corresponding to a classical de Sitter universe, which found an almost perfect agreement. We have repeated the analysis for various points in the phase diagram, giving consistent results.

These results provide compelling evidence that the phases of low vertex density of both foliated and nonfoliated CDT quantum gravity have the same large-scale properties in the continuum limit and lie in the same universality class. Since apart from removing the *distinguished* time slicing we essentially left all other ingredients of the kinematics intact, this would imply that the presence or absence of a preferred

foliation in CDT is not a relevant ingredient. As remarked already in the introduction, the same is not true for Hořava–Lifshitz gravity [13]—to the extent that our nonperturbative, coordinate-free setup can be compared with this continuum formulation—where a fixed spatial foliation is essential. It does not mean that CDT, or suitable extensions like that studied in Ref. [37], cannot provide a framework suitable for studying anisotropic gravity models. Our results also conform with the expectation that in $2 + 1$ dimensions, the value of the parameter α is irrelevant from the point of view of the continuum theory.

Because of the strong similarities of the large-scale properties of CDT quantum gravity in $2 + 1$ and $3 + 1$ dimensions, it is plausible to conjecture that also in $3 + 1$ dimensions, the presence or absence of a direct-product structure of the triangulations does not influence the final outcome. If this is the case, one may want to stick with the simpler "standard" formulation of causal dynamical triangulations as a matter of convenience and computational simplicity, as we have already pointed out elsewhere [12].

ACKNOWLEDGMENTS

We thank J. Ambjørn for a critical reading of the manuscript. The authors' contributions are part of the research program of the Foundation for Fundamental Research on Matter (FOM), financially supported by the Netherlands Organisation for Scientific Research (NWO). The work was also sponsored by NWO Exacte Wetenschappen (Physical Sciences) for the use of supercomputer facilities, with financial support from NWO.

[1] J. Ambjørn and J. Jurkiewicz, Phys. Lett. B **278**, 42 (1992).
[2] M. E. Agishtein and A. A. Migdal, Nucl. Phys. **B385**, 395 (1992).
[3] S. Catterall, J. B. Kogut, and R. Renken, Phys. Lett. B **328**, 277 (1994).
[4] P. Bialas, Z. Burda, A. Krzywicki, and B. Petersson, Nucl. Phys. **B472**, 293 (1996).
[5] B. V. de Bakker, Phys. Lett. B **389**, 238 (1996).
[6] J. Ambjørn and R. Loll, Nucl. Phys. **B536**, 407 (1998).
[7] R. Loll, Nucl. Phys. B, Proc. Suppl. **94**, 96 (2001); Lect. Notes Phys. **631**, 137 (2003); J. Ambjørn, J. Jurkiewicz, and R. Loll, *Approaches to Quantum Gravity*, edited by D. Oriti (Cambridge University Press, Cambridge, England, 2009), p. 341; R. Loll, Classical Quantum Gravity **25**, 114006 (2008); J. Ambjørn, A. Görlich, J. Jurkiewicz, and R. Loll, *Path Integrals—New Trends and Perspectives*, edited by W. Janke and A. Pelster (World Scientific, Singapore, 2008), p. 191; Acta Phys. Pol. B **39**, 3309 (2008); J. Ambjørn, J. Jurkiewicz, and R. Loll, Ann. Phys. (Amsterdam) **19**, 186 (2010); *Foundations of Space and Time*, edited by G. Ellis, J. Murugan, and A. Weltman (Cambridge University Press, Cambridge, England, 2012), p. 321; Proc. Sci., LATTICE2010 (2010) 014.
[8] J. Ambjørn, A. Görlich, J. Jurkiewicz, and R. Loll, Phys. Rep. **519**, 127 (2012).
[9] J. Ambjørn, J. Jurkiewicz, and R. Loll, Phys. Rev. Lett. **93**, 131301 (2004); Phys. Rev. D **72**, 064014 (2005).
[10] J. Ambjørn, A. Görlich, J. Jurkiewicz, and R. Loll, Phys. Rev. Lett. **100**, 091304 (2008); Phys. Rev. D **78**, 063544 (2008).
[11] J. Ambjørn, S. Jordan, J. Jurkiewicz, and R. Loll, Phys. Rev. Lett. **107**, 211303 (2011); Phys. Rev. D **85**, 124044 (2012).
[12] S. Jordan and R. Loll, Phys. Lett. B **724**, 155 (2013).
[13] P. Hořava, Phys. Rev. D **79**, 084008 (2009); Classical Quantum Gravity **28**, 114012 (2011); P. Hořava and C. M. Melby-Thompson, Phys. Rev. D **82**, 064027 (2010).
[14] J. Ambjørn, A. Görlich, S. Jordan, J. Jurkiewicz, and R. Loll, Phys. Lett. B **690**, 413 (2010).
[15] J. Ambjørn, L. Glaser, Y. Sato, and Y. Watabiki, Phys. Lett. B **722**, 172 (2013).
[16] J. Ambjørn, J. Jurkiewicz, and R. Loll, Nucl. Phys. **B610**, 347 (2001); Phys. Rev. Lett. **85**, 924 (2000).
[17] J. Ambjørn, A. Görlich, J. Jurkiewicz, R. Loll, J. Gizbert-Studnicki, and T. Trzesniewski, Nucl. Phys. **B849**, 144 (2011).
[18] J. Ambjørn, J. Jurkiewicz, and R. Loll, Phys. Rev. D **64**, 044011 (2001).
[19] D. Benedetti and J. Henson, Phys. Rev. D **80**, 124036 (2009).
[20] B. Durhuus and C. W. H. Lee, Nucl. Phys. **B623**, 201 (2002).
[21] F. Markopoulou and L. Smolin, Nucl. Phys. **B739**, 120 (2006).
[22] T. Konopka, Phys. Rev. D **73**, 024023 (2006).
[23] S. Jordan, Ph.D. thesis, Radboud University Nijmegen, 2013 (to be published).
[24] J. Ambjørn, J. Jurkiewicz, and R. Loll, in *Proceedings of the M-theory and Quantum Geometry, NATO Advanced Study Institute on Quantum Geometry, Akureyri, Iceland, 1999* (Kluwer, Dordrecht, Netherlands, 2000), p. 382; Lect. Notes Phys. **807**, 59 (2010); J. Ambjørn, A. Görlich, J. Jurkiewicz, and R. Loll, arXiv:1007.2560.
[25] B. Dittrich and R. Loll, Classical Quantum Gravity **23**, 3849 (2006).
[26] D. Benedetti and J. Henson, Phys. Lett. B **678**, 222 (2009).
[27] T. Regge, Nuovo Cimento **19**, 558 (1961).
[28] D. Benedetti, R. Loll, and F. Zamponi, Phys. Rev. D **76**, 104022 (2007).
[29] R. Hoekzema, Masters thesis, Utrecht University, 2012.
[30] R. Sorkin, Phys. Rev. D **12**, 385 (1975); **23**, 565(E) (1981).
[31] U. Pachner, Eur. J. Combinatorics **12**, 129 (1991).
[32] M. Gross and S. Varsted, Nucl. Phys. **B378**, 367 (1992).

[33] T. G. Budd and R. Loll, Phys. Rev. D **88**, 024015 (2013).
[34] G. Thorleifsson, Nucl. Phys. **B538**, 278 (1999).
[35] J. Ambjørn, D. V. Boulatov, A. Krzywicki, and S. Varsted, Phys. Lett. B **276**, 432 (1992); J. Ambjørn and S. Varsted, Nucl. Phys. **B373**, 557 (1992).
[36] J. Ambjørn, A. Görlich, J. Jurkiewicz, R. Loll, J. Gizbert-Studnicki, and T. Trzesniewski, Nucl. Phys. **B849**, 144 (2011).
[37] C. Anderson, S. J. Carlip, J. H. Cooperman, P. Hořava, R. K. Kommu, and P. R. Zulkowski, Phys. Rev. D **85**, 044027 (2012).